

# Microenvironment-responsive metal-phenolic network release platform with ROS scavenging, anti-pyroptosis, and ECM regeneration for intervertebral disc degeneration

Hao Zhou<sup>a,b,1</sup>, Jinpeng He<sup>a,1</sup>, Renfeng Liu<sup>a</sup>, Jun Cheng<sup>a</sup>, Yuhao Yuan<sup>c</sup>, Wanpu Mao<sup>b</sup>, Jun Zhou<sup>d</sup>, Honghui He<sup>b</sup>, Qianqi Liu<sup>a</sup>, Wei Tan<sup>a,\*</sup>, Cijun Shuai<sup>e,\*\*</sup>, Youwen Deng<sup>a,\*\*\*</sup>

<sup>a</sup> Department of Spine Surgery, The Third Xiangya Hospital, Central South University, Changsha, Hunan, 410013, China

<sup>b</sup> Department of Joint Surgery and Sports Medicine, The Affiliated Nanhua Hospital, Hengyang Medical School, University of South China, Hengyang, Hunan, 421002, China

<sup>c</sup> Department of Orthopedics, Xiangya Hospital, Central South University, Changsha, Hunan, 410008, China

<sup>d</sup> Institute of Medical Sciences, Xiangya Hospital, Central South University, Changsha, Hunan, 410008, China

<sup>e</sup> State Key Laboratory of High Performance Complex Manufacturing, College of Mechanical and Electrical Engineering, Central South University, Changsha, 410083, China

## ARTICLE INFO

### Keywords:

Intervertebral disc degeneration  
Metal-phenolic network  
Pyroptosis  
IL-17/ERK signaling pathway  
Reactive oxygen species

## ABSTRACT

Intervertebral disc degeneration (IVDD) can be caused by aging, injury, and genetic factors. The pathological changes associated with IVDD include the excessive accumulation of reactive oxygen species (ROS), cellular pyroptosis, and extracellular matrix (ECM) degradation. There are currently no approved specific molecular therapies for IVDD. In this study, we developed a multifunctional and microenvironment-responsive metal-phenolic network release platform, termed TMP@Alg-PBA/PVA, which could treat (IL-1 $\beta$ )-induced IVDD. The metal-phenolic network (TA-Mn-PVP, TMP) released from this platform targeted mitochondria to efficiently scavenge ROS and reduce ECM degradation. Pyroptosis was suppressed through the inhibition of the IL-17/ERK signaling pathway. These findings demonstrate the versatility of the platform. And in a rat model of IVDD, TMP@Alg-PBA/PVA exhibited excellent therapeutic effects by reducing the progression of the disease. TMP@Alg-PBA/PVA, therefore, presents clinical potential for the treatment of IVDD.

## 1. Introduction

Over two-thirds of the global population suffers from neck, shoulder, or lower back pains, which can negatively affect quality of life and health and impose socioeconomic burdens [1]. Intervertebral disc degeneration (IVDD) is a leading cause of these pains. Although conservative therapies can effectively alleviate pain, they do not slow the progression of IVDD [2]. Surgical interventions may increase the pressure on adjacent discs and exacerbate the risk of adjacent segment

disease [3]. Hundreds of clinical trials have been conducted to test drug candidates for the treatment of IVDD, but few have resulted in marked improvements in the disease. IVDD is a complex disease characterized by an array of pathological changes; therefore, single-target treatments are insufficient. Thus, for the effective treatment of IVDD, multi-target drug therapies need be urgently developed.

A growing body of evidence has suggested that IVDD is strongly associated with oxidative stress production, cellular pyroptosis, and extracellular matrix (ECM) degradation. Excess reactive oxygen species (ROS), mainly produced by mitochondria, may cause tissue damage

Peer review under responsibility of KeAi Communications Co., Ltd.

\* Corresponding author. Department of Spine Surgery, The Third Xiangya Hospital, Central South University, Changsha, Hunan, 410013, China.

\*\* Corresponding author. State Key Laboratory of High Performance Complex Manufacturing, College of Mechanical and Electrical Engineering, Central South University, Changsha, Hunan, 410083, China.

\*\*\* Corresponding author. Department of Spine Surgery, The Third Xiangya Hospital, Central South University, Changsha, Hunan, 410013, China.

E-mail addresses: [447067874@qq.com](mailto:447067874@qq.com) (H. Zhou), [drjinpenghe@163.com](mailto:drjinpenghe@163.com) (J. He), [524412608@qq.com](mailto:524412608@qq.com) (R. Liu), [chengjunductor@163.com](mailto:chengjunductor@163.com) (J. Cheng), [504807763@qq.com](mailto:504807763@qq.com) (Y. Yuan), [2451300458@qq.com](mailto:2451300458@qq.com) (W. Mao), [jz13549653156@126.com](mailto:jz13549653156@126.com) (J. Zhou), [hjh19731102@163.com](mailto:hjh19731102@163.com) (H. He), [8301180418@csu.edu.cn](mailto:8301180418@csu.edu.cn) (Q. Liu), [tanwei819@126.com](mailto:tanwei819@126.com) (W. Tan), [shuai@csu.edu.cn](mailto:shuai@csu.edu.cn) (C. Shuai), [drywdeng@csu.edu.cn](mailto:drywdeng@csu.edu.cn) (Y. Deng).

<sup>1</sup> The authors contributed equally to this work.

<https://doi.org/10.1016/j.bioactmat.2024.02.036>

Received 14 December 2023; Received in revised form 13 February 2024; Accepted 29 February 2024

2452-199X/© 2024 The Authors. Publishing services by Elsevier B.V. on behalf of KeAi Communications Co. Ltd. This is an open access article under the CC BY-NC-ND license (<http://creativecommons.org/licenses/by-nc-nd/4.0/>).

Abbreviations			
ABTS	2,2'-azino-bis-3-ethylbenzothiazoline-6-sulfonic acid	KEGG	Kyoto Encyclopedia of Genes and Genomes
Alg	alginate	LDH	lactate dehydrogenase
CCK-8	Cell Counting Kit-8	LPS	lipopolysaccharide;
Col-II	type II collagen	MRI	magnetic resonance imaging
DAPI	4',6-diamidino-2-phenylindole	NPCs	nucleus pulposus cells
DCFH-DA	dichloro-dihydro-fluorescein diacetate	NPs	nanoparticles
DEGs	differentially expressed genes	PBA	polyboronic acid
DHIs	disc height indices	PBS	phosphate-buffered saline;
DMPO	5,5-dimethyl-1-pyrroline N-oxide;	PI	propidium iodide;
DMSO	dimethyl sulfoxide;	PVA	polyvinyl alcohol
DPPH	2,2-diphenylpicrylhydrazyl	PVP	polyvinylpyrrolidone
ECM	extracellular matrix	ROS	reactive oxygen species
EDS	Energy-dispersive X-ray spectroscopy	RT-qPCR	real-time quantitative PCR
EPR	electron paramagnetic resonance	SD	Sprague-Dawley
FTIR	Fourier transform infrared spectroscopy	SEM	scanning electron microscopy
GO	Gene Ontology	TA	tannic acid
GSDMD-NT	N-terminal domain of GSDMD	TEM	transmission electron microscopy
HE	hematoxylin-eosin	TMP	TA-Mn-PVP
IVD	intervertebral disc	XO	xanthine oxidase
IVDD	intervertebral disc degeneration	XPS	X-ray photoelectron spectroscopy
		ERK	extracellular signal-regulated kinase

through oxidation reactions and initiation of inflammatory cascades. The imbalance between ROS production and clearance has been associated with poor prognoses in patients with IVDD [4]. The removal of excess ROS reduces the risk of IVDD [5,6]. Pyroptosis, a pro-inflammatory programmed cell death process, which can be induced by the inflammatory factor IL-1 $\beta$  and lipopolysaccharide. The continuous accumulation of inflammatory factors at the onset of IVDD has been found to induce pyroptosis in nucleus pulposus cells (NPCs) [7]. Upon the activation of cellular pyroptosis, caspase-1 cleaves the GSDMD protein into two structural domains: the N-terminus and C-terminus. The N-terminal domain of GSDMD (GSDMD-NT) binds to and perforates the plasma membrane, leading to cell membrane cleavage and cell death and ultimately causing the release of more pro-inflammatory cytokines [8]. In addition, ECM degradation in the inflammatory environment greatly contributes to IVDD progression [9]. In degenerating nucleus pulposus tissues with IVDD, type II collagen (Col-II) gradually transforms into type I collagen, and ECM-degrading enzymes are continuously secreted to promote tissue degeneration [10]. Given the critical roles of ROS, cellular pyroptosis, and the ECM in the pathogenesis of IVDD, the development of drugs that can simultaneously act on these targets is urgently needed to improve treatments for IVDD.

Several antioxidants have been developed to treat ROS-related diseases [11–13], including IVDD [14]; however, nanomaterials are more practical because of their better stability under physiological conditions, improved drug utilization, and longer-lasting effects than that of small-molecule compounds [15]. In addition, the use of nanoparticles (NPs) as drug delivery platforms is conducive to the use of multi-targeted and multifunctional therapies. However, most of the NPs that are currently used to treat diseases are metal based and can potentially introduce metal toxicity [16]. In addition, the mobility of nanosolutions limits their biomedical applications, particularly in disc injection therapy.

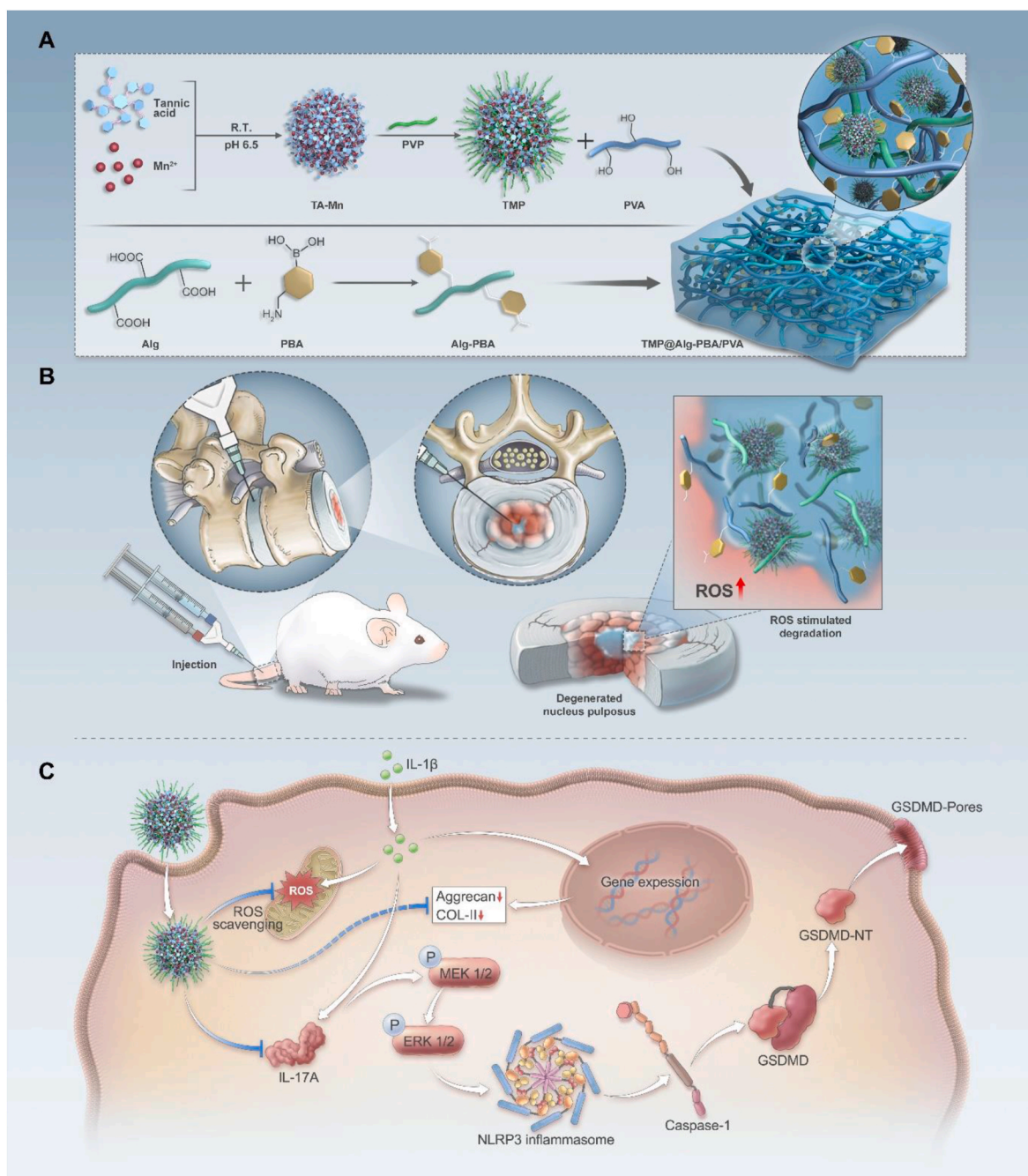
Tannic acid (TA), a phenolic hydroxyl-rich bioorganic compound, has gained attention owing to its anti-ROS and anti-inflammatory properties [17]. Kunzelmann et al. discovered the anti-pyroptotic effects of TA [18]. Recently, Mao et al. attributed this to the ability of TA to precisely target the mitochondria to scavenge ROS [19]. Sodium alginate (Alg) is a type of polysaccharide with good biocompatibility and adhesion, which has been commonly used as medical materials. Polyvinyl alcohol (PVA) is a kind of biodegradable polymer with high

hydrophilicity and good biocompatibility. Phenylboric acid (PBA) is a class of Lewis acids, which can react with *cis*-diol molecules to form dynamic borate ester bonds after ionization. Then, the borate ester bonds can break in response to ROS [20]. The objectives of the present study were to (1) develop a TA-derived metal-phenolic network (TA-Mn-PVP, TMP) with efficient ROS-scavenging activity that could target mitochondria through a simple self-assembly process using TA, manganese, and polyvinylpyrrolidone (PVP) as raw materials, and evaluate its efficacy against IL-1 $\beta$ -induced IVDD (Scheme 1); (2) load the TMP onto an ROS-responsive release platform (TMP@Alg-PBA/PVA) to reduce the possibility of damage to critical sites, such as the spinal cord, while efficiently utilizing NPs; and (3) assess the anti-pyroptotic effects of the platform and its multifunctional properties to achieve the synergistic treatment of IVDD. The study provides evidence of the clinical potential of TMP@Alg-PBA/PVA in the synergistic treatment of IVDD via on-demand NPs release, scavenging ROS, inhibiting cellular pyroptosis and reducing ECM degradation.

## 2. Materials and methods

### 2.1. Clinical tissue samples

The experimental protocol was approved by the Ethics Committee of the Affiliated Nanhua Hospital, University of South China (2023-KY-61). Degenerated nucleus pulposus tissues from patients who had undergone IVDD surgery. Nine patients (5 males and 4 females) aged between 36 and 64 years were included in the study. The selected patients were independently diagnosed by two or more experienced associate physicians, and the diagnoses were confirmed by a highly qualified chief physician. The inclusion criteria included: 1) medical histories and imaging findings that met the diagnostic criteria and had Pfirrmann ratings of III or higher; 2) symptoms that remained unrelieved after more than 3 months of conservative treatment; 3) informed consent obtained for both surgical treatments and participation in the study. The exclusion criteria were: 1) infections in the vertebral body or adjacent areas and 2) ineligibility for surgery due to other underlying diseases. Preoperative information, including magnetic resonance imaging (MRI) examination results, was collected from all patients. Nucleus pulposus tissues obtained during surgery were promptly fixed with 4% paraformaldehyde. Subsequently, the tissues were sectioned, stained, and subjected to semi-



**Scheme 1.** Schematic representation of the multifunctional and microenvironment-responsive metal-phenolic network release platform for IVDD treatment. A) Preparation process of the nanoparticle-laden ROS-responsive hydrogel platform. B) Application of the TMP@Alg-PBA/PVA release platform to inflamed areas within the IVDD. C) Therapeutic mechanisms of the TMP@Alg-PBA/PVA release platform.

quantitative analysis using ImageJ software.

## 2.2. Nanoparticle preparation

Two solutions of TA (Aladdin, Shanghai, China) and  $\text{MnCl}_2 \cdot 4\text{H}_2\text{O}$  (Macklin, Shanghai, China) were initially prepared.  $\text{MnCl}_2 \cdot 4\text{H}_2\text{O}$  (40 mg) was dissolved in 8 mL of water, and TA (10 mg) was dissolved in 1 mL of water. The TA solution was gradually added to the  $\text{MnCl}_2 \cdot 4\text{H}_2\text{O}$  solution at 25 °C at a 1:8 vol ratio with vigorous stirring. After 1 h, the pH was adjusted to approximately 6.5 using sodium hydroxide to achieve the desired color change. Subsequently, an aqueous solution of PVP (Aladdin, Shanghai, China), with a concentration of 66 mg/mL and an average molecular weight of 30 kDa, was introduced into the solution

and subjected to sonication for 10 min. Upon the completion of the reaction, TMP NPs were obtained after centrifugation for 15 min, followed by three washes with ultrapure water.

## 2.3. Characterization of TMP NPs

The morphology and elemental composition of the TMP NPs were characterized using transmission electron microscopy (TEM; FEI Tecnai F20, USA) and scanning electron microscopy (SEM; Zeiss Sigma 300, Germany). Fourier transform infrared spectroscopy (FTIR; Thermo Fisher Nicolet iN10, USA) was used to observe the coordination between TA and  $\text{Mn}^{2+}$ . The zeta potential and average hydrodynamic particle diameter were determined using a Malvern Zetasizer Nano Series

instrument (Nano ZS90, UK). The chemical composition and ionic valence states of TMP were analyzed using X-ray photoelectron spectroscopy (XPS; ESCALAB250Xi, Thermo Scientific, USA) with an Al K $\alpha$  source (1486.6 eV). The drug content of the TMP NPs was quantified using a thermogravimetric analysis (TGA5500). To quantify the manganese content in the NPs, TMP was pre-treated with aqua regia, and the manganese content was determined using inductively coupled plasma mass spectrometry (Agilent 7500C, USA). To observe the stability of the NPs, the TA and TMP NPs powders were dissolved in dimethyl sulfoxide (DMSO) and simulated body fluid, then placed in sunlight (25 °C). Two hundred microliters of the solution was collected every 24 h, and the remaining TA content was measured using a UV–Vis spectrophotometer.

#### 2.4. Depletion of ROS by TMP NPs

The overall antioxidant capacity of the TMP NPs was determined using a Total Antioxidant Capacity Assay Kit (ABTS method; Beyotime, Shanghai, China). This assay used 2,2'-azino-bis-3-ethylbenzothiazoline-6-sulfonic acid (ABTS) as the chromogenic reagent. In the ABTS assay, ABTS<sup>•+</sup> is formed upon oxidation, thus maintaining the stability of water or acidic ethanol. The addition of an antioxidant prompts ABTS<sup>•+</sup> to react, leading to discoloration [21]. The absorbance of ABTS<sup>•+</sup> was measured at the maximum absorption wavelength (734 nm) using a UV–Vis spectrophotometer. In addition, a 2,2-diphenylpicrylhydrazyl (DPPH) free radical test solution was prepared by dissolving DPPH in ethanol [22]. Varying concentrations of the TMP solution were added to the DPPH free radical test solution, followed by a 30 min incubation period in the dark. The absorbance at 517 nm was measured to determine the scavenging efficiency. An Fe<sup>2+</sup>/H<sub>2</sub>O<sub>2</sub> system was used to generate •OH. The ability of TMP NPs (50 µg/mL) to quench •OH was investigated via electron paramagnetic resonance (EPR), with 5,5-dimethyl-1-pyrroline N-oxide (DMPO) as the spin probe. The xanthine/xanthine oxidase (XO) system was used to generate O<sub>2</sub><sup>•-</sup>. The ability of the TMP NPs (50 µg/mL) to quench O<sub>2</sub><sup>•-</sup> was then assessed using EPR, with DMPO as the O<sub>2</sub><sup>•-</sup> trapping agent.

#### 2.5. Preparation of the hydrogel

Two grams of Alg (Macklin, Shanghai, China) and 0.78 g of PBA (Aladdin, Shanghai, China) were dissolved in 200 mL of deionized water. 1.96 g of EDC-HCl (Aladdin, Shanghai, China) was then added, after which the mixture was stirred overnight at 25 °C. After the reaction had taken place, the mixture underwent a 3 day dialysis period in deionized water using dialysis bags, with a molecular weight cut-off of 8–14 kDa (Biosharp, Beijing, China). The resulting mixture was freeze dried to produce Alg-PBA. A specific concentration of the TMP NPs was mixed with PVA (Macklin, Shanghai, China) in an aqueous solution and sonicated for 10 min. This mixture was added directly to the Alg-PBA solution. The hydrogel was formed within a few seconds. Notably, the reticulated hydrogel platform exhibited ROS responsiveness through the borate bond formed between the PBA and PVA [20].

#### 2.6. Characterization of the TMP@Alg-PBA/PVA release platform

To validate the successful synthesis of the hydrogel and assess its rheological properties, FTIR spectroscopy and a rheometer (TA Instruments DHR-2, USA) were used. The hydrogel was freeze-dried for 24 h, sputter-coated with gold, and examined using SEM (ZEISS Sigma 300, Germany) to analyze the microstructure of the material surface. Energy-dispersive X-ray spectroscopy (EDS) mapping of the TMP@Alg-PBA/PVA hydrogel was then conducted. The hydrogel system was sequentially tested for self-healing, moldability, injectability, and rheology. To test the ROS-responsive degradability of the hydrogel system, two identical volumes of rhodamine-B pre-stained hydrogels were placed into separate containers: one containing phosphate-buffered saline (PBS) and the other containing a PBS solution with an H<sub>2</sub>O<sub>2</sub>

concentration of 50 µM, 100 µM, 200 µM and 400 µM. Degradation was observed after 0, 12, 24, and 48 h. To study the release kinetics of the NPs from this platform, we collected solutions after 0, 10, 20, 40, 60 min and 3, 6, 12, 24 h and quantified the samples by measuring the absorbance with a UV–Vis spectrophotometer (PE lambda 750, USA).

#### 2.7. Cell preparation and characterization in vitro

NPCs were obtained from 6-week-old male Sprague-Dawley (SD) rats (SJA, Hunan, China). Following isolation, primary cells were cultured in complete DMEM/F12 medium (Gibco, USA) and characterized using Alcian Blue staining and immunofluorescence with a Col-II antibody (Immunoway, Jiangsu, China), as shown in Fig. S1. Subsequent experiments used these cells after they had been passaged for three generations.

#### 2.8. Co-culture system and cell viability assessment

Following the TMP@Alg-PBA/PVA hydrogel treatment, cell viability was assessed using a Cell Counting Kit-8 (CCK-8) assay (Beyotime, Shanghai, China). Cells were seeded at a density of  $5 \times 10^3$  cells/well in 96-well plates (NEST, Jiangsu, China) and cultured with the TMP@Alg-PBA/PVA hydrogel extract, which was immersed in DMEM/F12 media containing 10% fetal bovine serum (Bioind, Israel) and 1% penicillin/streptomycin (Procell, Wuhan, China) for 24 h. Subsequently, 100 µL of fresh complete culture medium, containing 10 µL of the CCK-8 reagent was added, and the solution was incubated at 37 °C for 2 h. The Blank groups contained no cells with the medium and CCK-8 reagents, and the Control groups included untreated cells. Cell viability was determined by measuring the absorbance at 450 nm using a Thermo Varioskan Flash microplate reader. Co-culture experiments were performed using Transwell-Permeable Support (Corning Incorporated, USA), with polyester membranes consisting of 0.4-µm pore sizes. NPCs at a concentration of  $1.5 \times 10^4$ /mL were placed in the lower chamber, while the hydrogel was positioned in the upper chamber. On days 1 and 3, the cells were incubated with 250 µL of Calcein-AM/propidium iodide (PI) detection working solution (Beyotime, Shanghai, China) for 30 min. Subsequently, the cells were examined under a fluorescence microscope. Live, intact cells displayed green fluorescence, and cells with damaged membranes appeared red.

#### 2.9. Antioxidant properties, cellular uptake, lysosome escape, and mitochondrial targeting

Intracellular ROS levels were evaluated by staining with 5 µM dichloro-dihydro-fluorescein diacetate (DCFH-DA; MCE, USA) for 10 min, followed by fluorescence microscopy and flow cytometry for quantification. Alterations in the mitochondrial membrane potential were evaluated using a JC-1 fluorescent probe kit (AbMole, Shanghai, China). Observations were made using a Leica N2-Dmi8 fluorescence microscope, and a semi-quantitative analysis was performed using ImageJ software. To assess the uptake efficiency of TMP by the NPCs, the TMP NPs were labeled with CY5 fluorescence (Coolaber, Beijing, China). The NPCs were then co-cultured with TMP@Alg-PBA/PVA for different time periods and at different TMP concentrations. Subsequently, the cells were fixed with 4% paraformaldehyde, rinsed three times with PBS and stained with 4',6-diamidino-2-phenylindole (DAPI; Solarbio, Beijing, China) to observe the nuclei. The stained cells were examined using a laser confocal microscope with the DAPI excitation wavelength at 350 nm and the CY5 excitation wavelength at 650 nm. A flow cytometry analysis was performed after harvesting cells from six-well plates within a designated time frame and with ethylenediaminetetraacetic acid-free trypsin digestion. Subsequently, the cells were filtered through a 200-mesh sieve into Eppendorf tubes, washed three times with flow buffer, and stored at 4 °C. Flow cytometry was performed to quantify the fluorescence intensity of CY5 in each group. To confirm the location of

the TMP NPs in the lysosomes and mitochondrial regions,  $2 \times 10^4$  cells/well were seeded in 24-well plates. When cellular confluence reached 70%, co-cultivation was initiated using TMP@Alg-PBA/PVA loaded. Lysosomes were stained with a lysosome staining kit (Beyotime, Shanghai, China), and the nuclei were stained with Hoechst (Solarbio, Beijing, China). The stained samples were subjected to confocal laser microscopy (ZEISS LSM 900, Germany), and a co-localization analysis was performed using ImageJ.

### 2.10. *In vitro* NPCs pyroptosis model and evaluation of anti-pyroptotic effects

Unlike the conventional use of lipopolysaccharide (LPS) or peroxides, such as  $H_2O_2$ , as inducers in pyroptosis models, we selected IL-1 $\beta$  as the inducer, given the significant role of IL-1 $\beta$  in triggering intervertebral disc (IVD) pyroptosis [23] and the documented modeling of pyroptosis in NPCs by IL-1 $\beta$  [24]. Furthermore, LPS, which originates from bacterial cell walls, has been found to induce non-classical pyroptosis models [25]. Given that IVDD primarily occurs under aseptic conditions and is associated with classical pathway-related pyroptosis [26], we excluded LPS. As potent oxidizing agents, peroxides can directly react with our TMP NPs, which have robust reducing properties [27], thereby potentially affecting the modeling process, which may obscure the direct effects of the NPs on pyroptosis. Therefore, NPCs were co-cultured with the TMP@Alg-PBA/PVA hydrogel for 24 h, followed by a 24-h intervention with IL-1 $\beta$  (Novoprotein, Shanghai, China).

The cell status was assessed using a CCK-8 assay, lactate dehydrogenase (LDH) cytotoxicity assay (Beyotime, Shanghai, China), and Calcein-AM/PI staining. Immunofluorescence staining was performed to evaluate the expression of NLRP3, caspase-1, and GSDMD-NT. Cell slides were fixed with 4% paraformaldehyde, permeabilized using 0.5% Triton X-100, and blocked with 5% bovine serum albumin. The slides were then incubated with primary antibodies targeting NLRP3 (CST, USA), caspase-1 (Sigma, USA), and GSDMD-NT (Immunoway, Jiangsu) for 24 h at 4 °C. The following day, the cells were washed with PBS, treated with a fluorescent secondary antibody (Immunoway, Jiangsu, China), and stained with DAPI. Visualization was performed using confocal laser microscopy. Expression analyses of the NLRP3, caspase-1, GSDMD, and GSDMD-NT proteins were performed using western blotting with GAPDH (Immunoway, Jiangsu) as the reference protein, and the protein marker was purchased from Vazyme, MP102-02. Real-time quantitative PCR (RT-qPCR) with fluorescence detection was used to measure the expression of IL-1 $\beta$  and TNF- $\alpha$ . Relative gene expression was calculated using the  $2^{-\Delta\Delta Ct}$  method. Gene-specific primers were synthesized by Sango Biotech, Shanghai, China, as detailed in Table S1.

### 2.11. Observation of cell membrane morphology by SEM

Following fixation with 2.5% glutaraldehyde, the cells underwent a series of processing steps. The fixative was discarded, and the samples were thoroughly rinsed thrice with PBS, with each wash lasting 15 min. Subsequently, the samples were fixed using a 1% osmium solution for 1–2 h. After the careful removal of the osmium waste solution, the samples underwent three additional rinses with PBS, each lasting 15 min. Dehydration was achieved through sequential immersion in graded ethanol solutions, including 30%, 50%, 70%, 80%, 90%, and 95%, with each concentration applied for 15 min. This was followed by two immersions in 100% ethanol, each lasting 20 min. The samples were treated with a mixture of ethanol and isoamyl acetate (V/V = 1/1) for 30 min, followed by treatment with pure isoamyl acetate for 1 h. Critical point drying was then performed. Subsequently, the cells were coated and visualized using SEM.

### 2.12. Transcriptomic analysis

To assess the gene-level changes in the NPCs, we divided the NPCs into two groups: one group received a 40  $\mu$ g/mL IL-1 $\beta$  treatment (N = 3), and the other was co-cultivated with 200  $\mu$ g/mL TMP@Alg-PBA/PVA (N = 3) before the IL-1 $\beta$  treatment. Total RNA was extracted using TRIzol Reagent (Invitrogen Life Technologies, USA), and its concentration, quality, and integrity were assessed using a NanoDrop spectrophotometer (Thermo Scientific, USA). High-throughput sequencing was performed by Shanghai Personal Biotechnology Co., Ltd. The sequencing library was processed using the Illumina NovaSeq 6000 platform. A differential expression analysis between two comparison combinations was performed using DESeq (v1.38.3) software. A Gene Ontology (GO) enrichment analysis was conducted using Top GO (v2.50.0), and *P*-values were calculated using the hypergeometric distribution method. Significantly enriched GO terms for the differentially expressed genes (DEGs; upregulated or downregulated) were identified based on a *P*-value < 0.05. The hypergeometric distribution test was applied to the Kyoto Encyclopedia of Genes and Genomes (KEGG) pathway analysis. To verify the role of the screened pathways in the process of pyroptosis in NPCs, we intervened the NPCs with an IL-17 inhibitor (MedChemExpress, USA), and subsequently detected the expression of the IL-17 signaling pathway-related proteins IL-17A (Bioss, Beijing), MEK1/2, pMEK1/2, ERK1/2, and pERK1/2 (Zen-bio, Chengdu).

### 2.13. Evaluation of ECM degradation

Immunofluorescence staining was used to assess the expression of Col-II and aggrecan (Zen-bio, Sichuan, China) in the NPCs. Western blotting was used to evaluate the expression of Col-II, aggrecan, MMP-3 (Proteintech, Wuhan), MMP-13 (Proteintech, Wuhan), and GAPDH (Immunoway, Jiangsu). Subsequently, RT-qPCR with fluorescence detection was performed to assess the expression of ECM-related genes. Expression was analyzed using the  $2^{-\Delta\Delta Ct}$  method.

### 2.14. Establishment of IVDD rat models

Six-week-old male SD rats were used to establish a caudal IVDD model. The Ethics Committee of the Department of Animal Experimentation at Central South University (CSU-2023-0436) approved the animal experimental protocol. The rats were obtained from Hunan Slake Jingda Experimental Animal Co., Ltd. Surgical instruments were sterilized at high temperatures and pressures. After anesthesia, a 5  $\mu$ L solution of IL-1 $\beta$  (40  $\mu$ g/mL) was injected into the IVD located between the Co7-8 intervertebral spaces in the tails of the rats, using a 21G needle and microsyringe, except sham-operated group. Three days later, the Control group received a 10  $\mu$ L PBS injection, and the Gel group received an injection of 10  $\mu$ L of Alg-PBA/PVA. The Low group was injected with 10  $\mu$ L of TMP@Alg-PBA/PVA containing 100  $\mu$ g/mL of TMP, and the High group received an injection of 10  $\mu$ L of TMP@Alg-PBA/PVA containing 200  $\mu$ g/mL of TMP. The rats were euthanized after 4 and 8 weeks, and IVD specimens were collected for analysis.

### 2.15. Imaging evaluation

After euthanizing the rats, radiographic and MRI examinations were performed on the rat tails. X-ray imaging was used to calculate the changes in the disc-height index (DHI) for the treated discs, expressed as DHI%, which were then compared to those of the initial undegenerated normal discs. MRI assessment-graded disc degeneration was performed using the Pfirrmann grading system, which relies on T2-weighted slice imaging.

## 2.16. Histological evaluation

Tissue samples were collected after 4 and 8 weeks, decalcified for 1 month, and embedded in paraffin. The specimens were sectioned into 3- $\mu\text{m}$  slices with a sectioning machine. Internal histological changes in the discs were assessed using hematoxylin-eosin (HE) and Safranin O-Fast Green staining. Immunohistochemistry was used for the quantitative assessment of the ECM, and immunofluorescence was used to measure pyroptosis-related protein expression.

## 2.17. Statistical analyses

All quantitative data ( $N \geq 3$ ) are expressed as the mean  $\pm$  standard deviation. Data were analyzed using SPSS25, GraphPad Prism, and Origin software. Statistical analyses included one-way analysis of variance with Tukey's multiple comparisons tests to assess intergroup differences. Statistical significance was defined as  $P < 0.05$ .

## 3. Results and discussion

### 3.1. Observation of the pathological changes in human IVDD tissue samples

To better understand the pathological changes that occur in tissues at the onset of IVDD, we collected nucleus pulposus tissues specimens from patients with IVDD (Fig. 1A); patient information is shown in Table S2. Fig. 1B shows MRI images of the three levels of IVDD, labeled with arrows pointing to the degenerate location. As degeneration progresses, IVD dehydration worsens, and the T2-weighted signal decreases, eventually leading to the narrowing or loss of the intervertebral space. Safranin O-Fast Green staining revealed decreasing cell numbers in the nucleus pulposus tissues and increasing disorganization and fibrosis of the ECM as degeneration advanced (Fig. 1C); this result was also confirmed using HE staining (Fig. S2). The immunohistochemical and semi-quantitative results in Fig. 1D and F shows a significant reduction in Col-II and aggrecan protein expression in degenerative IVD tissues with high Pfirrmann grades, suggesting tissue water loss and development of fibrotic lesions.

As an inflammatory mechanism of cell death, pyroptosis contributes to the development of several diseases. To explore the key role of pyroptosis in IVDD, the expression of crucial pyroptosis-related proteins, including the NLRP3 inflammasome, caspase-1, and IL-1 $\beta$ , was assessed in IVD tissues. In tissues categorized according to the Pfirrmann classification, these three proteins were highly expressed in grade V, followed by grade IV; the proteins in grade III exhibited the lowest expression (Fig. 1E). Additionally, a semi-quantitative analysis of the histological findings demonstrated that the increased expression of pyroptotic proteins was associated with higher grades (Fig. 1G). These results suggest that pyroptosis promotes IVDD progression. ROS, which are closely associated with pyroptosis and ECM degradation, have been found to play an equally important role in the development of IVDD [28]. The presence of ROS promotes cellular pyroptosis and ECM degradation. Thus, ROS removal is equally crucial in treating IVDD.

### 3.2. Characterization of TMP NPs

A stable solution of TMP NPs was obtained through the construction of a TA-Mn (TM)-coordinated metal-polyphenolic network through the self-assembly of  $\text{Mn}^{2+}$  with TA, followed by TM surface modification with PVP (Fig. 2A). The synthesis step is straightforward, cost-effective, and easily executed without the need for a complex environment, such as high temperatures or high pressure; hence, it is well-suited for the large-scale synthesis [29]. The synthesis was verified by FTIR, and the vibrational and substitution bands of the benzene ring appeared near 1550  $\text{cm}^{-1}$  and 790  $\text{cm}^{-1}$ , respectively. In addition, the vibrational peaks at 1300–1600  $\text{cm}^{-1}$ , 1700  $\text{cm}^{-1}$ , and 3600  $\text{cm}^{-1}$  corresponded to

the O–C–O, C=O, and O–H functional groups, respectively, confirming the successful synthesis of TMP (Fig. 2B). The shapes and sizes of the TMP were determined through SEM and TEM images. The average hydrodynamic particle diameter was mainly concentrated at approximately 180 nm (Fig. 2C and D). As shown in the elemental mapping diagram, the NPs were mainly composed of carbon and oxygen (Fig. 2E). The TMP loading content was determined using a thermogravimetric analysis, which revealed that the content of organic components in the TMP NPs exceeded 73.2% (Fig. 2F). This illustrated the high drug loading of the NPs. To study the stabilities of TA and TMP, each was dissolved in DMSO and simulated body fluid at 25  $^{\circ}\text{C}$  for 23 days, after which TA degradation was quantified using a UV–Vis spectrophotometer. The degradation of TA in TMP was significantly attenuated, thereby effectively preserving the stability of the drug over an extended duration. Conversely, TA degraded rapidly in DMSO and simulated body fluids (Fig. 2G–S3 and S4). This may have been because the presence of manganese and PVP greatly improved the stability of TA, acting as a coordinator and increasing bioavailability [30].

Zeta potential measurements demonstrated the negatively charged nature of the TMP NPs in different solvents. Notably, no significant difference in stability was observed between TMP in water and PBS (1x), as reflected by zeta values of  $-19.1$  mV and  $-18.5$  mV, respectively. Although the zeta value slightly increased to  $-12$  mV in the DMEM/F12 solution, it still indicated the favorable stability of TMP (Fig. 2H). Full scanning spectroscopy confirmed that the TMP NPs were mainly composed of carbon (68.88%), oxygen (24.62%), nitrogen (5.88%), and manganese (0.6%) (Fig. 2I). Generally, transition metals combined with polyphenols to form metal-polyphenolic networks often exhibit unwanted toxicity owing to the high concentration of toxic metals [31]. However, in this study, the synthesized TMP metal-polyphenolic networks had a low  $\text{Mn}^{2+}$  concentration, which minimized the potential metal toxicity of the NPs for *in vivo* application [32–34]. A further analysis of the indicated compositions, using XPS, revealed that C=O, C–O, and Mn–O species were present in the NPs. The manganese on the surface of TMP was predominantly divalent, trivalent, or tetravalent (Fig. 2J and K). Notably, studies have shown that the release of  $\text{Mn}^{2+}$  can accelerate collagen recycling and efficient ECM remodeling [35], and the presence of  $\text{Mn}^{3+}$  and  $\text{Mn}^{4+}$  facilitates efficient ROS elimination [36]. In conclusion, the synthesis of TMP is hypotoxic, and its products are stable in various solution environments, with high drug loading and slow drug degradation rates.

### 3.3. ROS-scavenging activity of TMP NPs

After characterizing the TMP NPs, their ROS-scavenging abilities were explored. Radical-scavenging activity was assayed using ABTS and DPPH probes. ABTS was oxidized in the presence of  $(\text{NH}_4)_2\text{S}_2\text{O}_8$  to produce stable  $\text{ABTS}^{+\bullet}$ , which appeared blue and exhibited a characteristic UV–Vis absorbance peak at  $\sim 734$  nm. The addition of the TMP NPs was effective in reducing the UV–Vis absorbance, and the dark blue color was further diminished (Fig. 3A). The free radical-scavenging rate was assessed, which revealed that more than 70% of free radicals were scavenged, following the use of 100  $\mu\text{g}/\text{mL}$  TMP NPs (Fig. 3B). DPPH $\bullet$  had a strong UV–Vis absorbance peak at  $\sim 525$  nm. Similarly, after incubation with the TMP NPs, the UV–Vis absorbance decreased in a concentration-dependent manner, and the color of the solution changed from purple to orange (Fig. 3C), indicating the gradual scavenging of free radicals. Statistical analyses corroborated this observation, revealing that TMP at a concentration of 100  $\mu\text{g}/\text{mL}$  exhibited DPPH removal rates more than four times faster than that at 12.5  $\mu\text{g}/\text{mL}$  (Fig. 3D). These results suggest that the TMP NPs exhibit a concentration-dependent free radical-scavenging rate and ability.

$\bullet\text{OH}$  and  $\text{O}_2^{\bullet-}$  are reactive oxygen radicals that can lead to DNA damage and protein breakage, thereby causing tissue damage and degeneration [37–39]. Therefore, the scavenging activities of the TMP NPs for  $\bullet\text{OH}$  and  $\text{O}_2^{\bullet-}$  were investigated. An  $\text{O}_2^{\bullet-}$ -generating

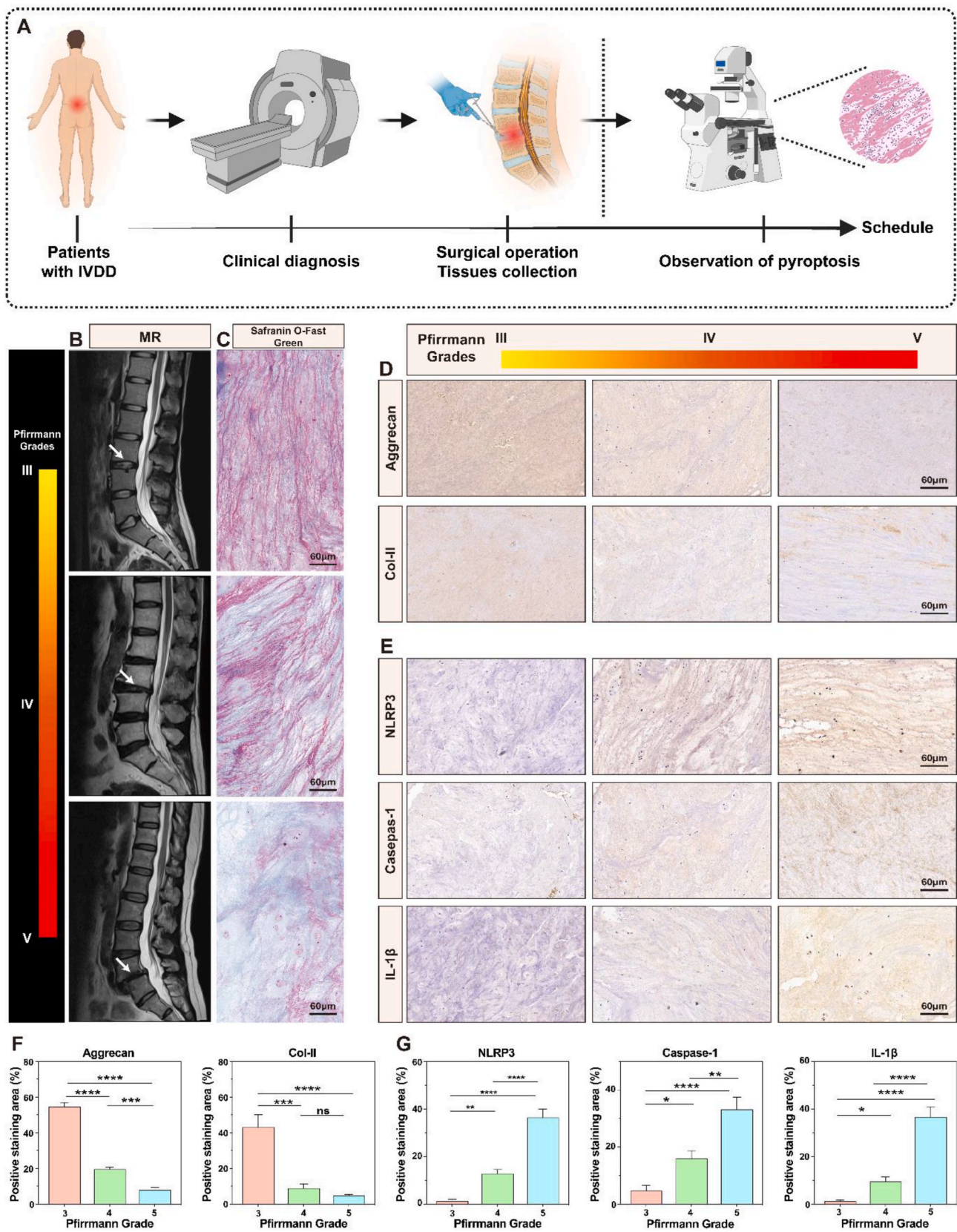
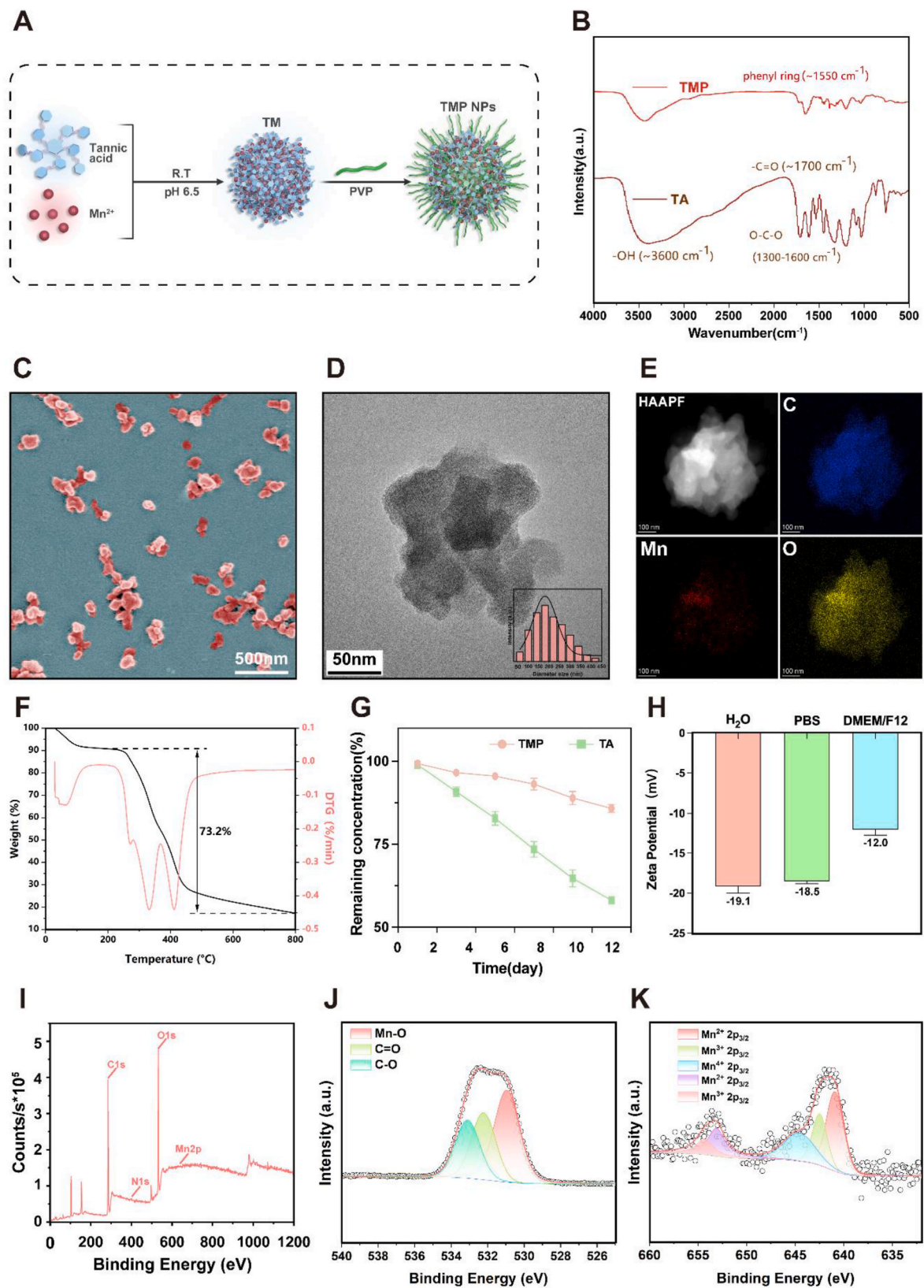
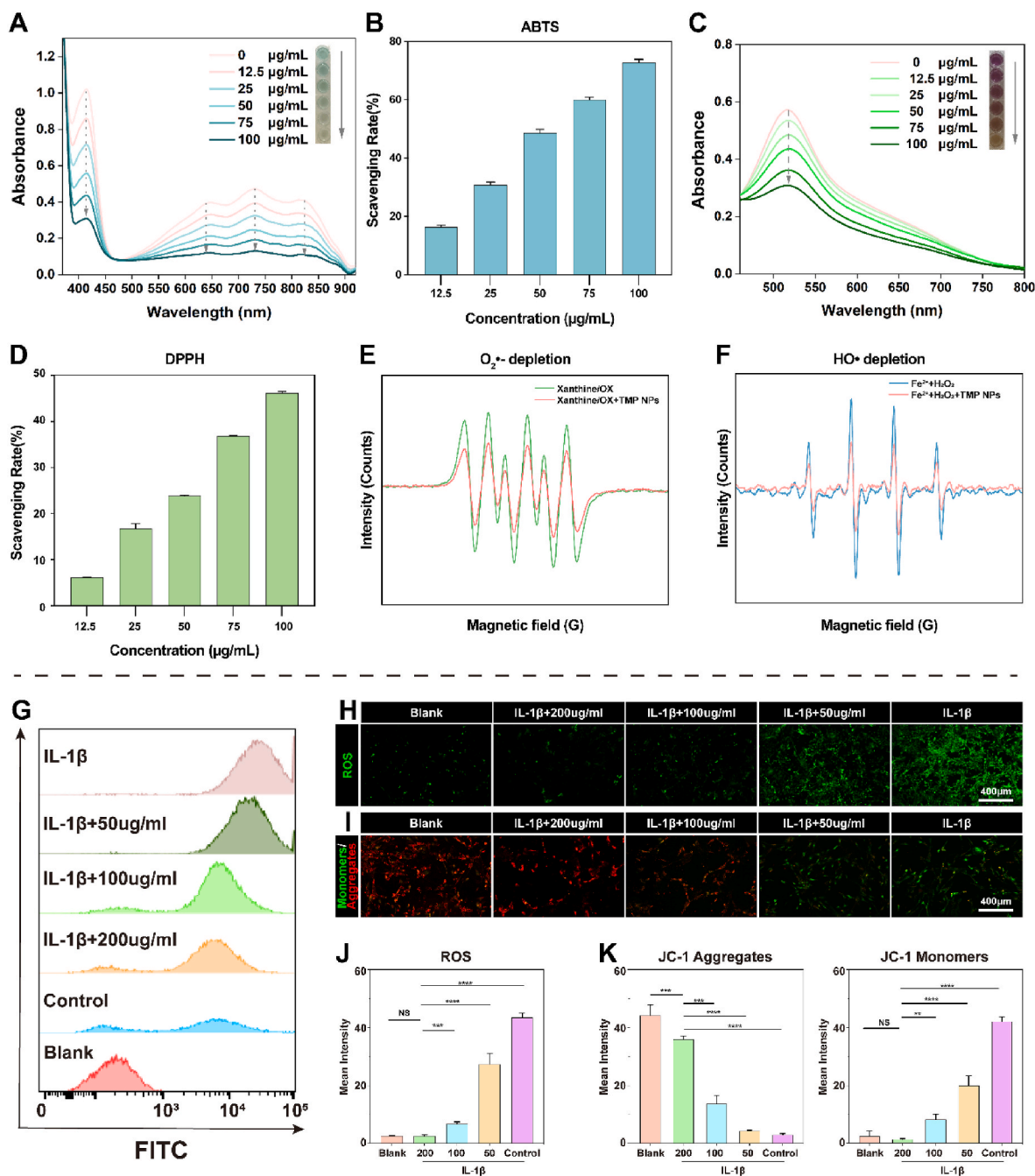


Fig. 1. Pathological changes in clinical degenerate IVD samples. A) Scheme of the clinical sample collection. B) MRI images categorized as Pfirrmann grades III, IV, and V. C) IVD tissue samples stained with Safranin O-Fast Green. D) Histological staining of IVD tissues for an analysis of Col-II and aggrecan expression. E) Histological staining of IVD specimens for pyroptosis-related proteins NLRP3, caspase-1, and IL-1β. F) Semi-quantitative analysis of Col-II and aggrecan expression. G) Semi-quantitative analysis of NLRP3, caspase-1, and IL-1β. \* $P < 0.05$ , \*\* $P < 0.01$ , \*\*\* $P < 0.001$ , \*\*\*\* $P < 0.0001$  vs. Pfirrmann grades III. NS vs. Pfirrmann grades III, not significant. N = 3.



**Fig. 2.** Synthesis and characterization of TMP NPs. A) Schematic of the synthesis of TMP NPs. B) FTIR spectra displaying TA and TMP patterns. C) SEM image of the TMP NPs. D) TEM images of the TMP NPs. Inset: Average hydrodynamic particle diameter of the TMP NPs. E) Elemental mapping microscopy images of the TMP NPs. F) Thermogravimetric analysis of the TMP NPs. G) TA and TMP degradation curves. H) Zeta potential values for the TMP NPs in various solvents. I–K) Full scan XPS survey spectrum (I) and the high-resolution spectra for the O1s (J) and Mn2p(K) of TMP. N = 3.



**Fig. 3.** ROS-scavenging activity of the TMP NPs. A, C) UV–Vis absorbance spectra of (A) ABTS<sup>•+</sup> and (C) DPPH<sup>•</sup> exposure with different concentrations of TMP NPs. Inset: Photographs of the color of each reaction solution. B, D) Histograms of the scavenging ratios of (B) ABTS<sup>•+</sup> and (D) DPPH<sup>•</sup> with different concentrations of TMP. E) O<sub>2</sub><sup>•-</sup> and F) •OH depletion capacities of the TMP NPs, determined using EPR. G) Flow cytometry results showing the ability of TMP to scavenge ROS after IL-1β treatment. H) Alleviation of oxidative stress in NPCs after different treatments monitored by DCFH-DA. I) JC-1 fluorescence was used to monitor mitochondrial membrane potential changes in NPCs. Green fluorescence indicates that mitochondrial membrane potential is low, and JC-1 is in a monomer state, while red fluorescence indicates that the mitochondrial membrane potential is high, and JC-1 forms aggregates. J) Semi-quantitative analysis of ROS fluorescence performed using ImageJ. K) Semi-quantitative analysis of JC-1 mitochondrial membrane potential. \**P* < 0.05, \*\**P* < 0.01, \*\*\**P* < 0.001, \*\*\*\**P* < 0.0001 vs. Blank group. NS vs. Blank group, not significant.

xanthine/XO system with DMPO was used as the spin probe and the EPR method was used to investigate the O<sub>2</sub><sup>•-</sup> scavenging capacity. The DMPO/O<sub>2</sub><sup>•-</sup> showed a strong characteristic signal peak of the xanthine/XO system (Fig. 3E); following the addition of the TMP NPs (50 µg/mL), the signal intensity decreased significantly, indicating that the TMP NPs have good O<sub>2</sub><sup>•-</sup> scavenging activity. The •OH depletion ability of the TMP NPs was investigated using EPR with DMPO as the probe. •OH was initially produced by the Fe<sup>2+</sup>/H<sub>2</sub>O<sub>2</sub> reaction system, which

exhibited a clear •OH EPR signal (Fig. 3F). The addition of the TMP NPs (50 µg/mL) caused a sharp decrease in the •OH signal intensity, indicating that the treatment with low-dose TMP NPs reduced •OH.

After characterizing the ROS-scavenging performance of the NPs for ROS at the chemical level, we observed the ROS-scavenging performance in cells. The excellent biocompatibility of NPs is a prerequisite basis for biological or clinical applications. Previous studies have shown that TMP NPs up to 200 µg/mL have little effect on cell viability

(Fig. S5). Therefore, we used 200  $\mu\text{g}/\text{mL}$  of TMP NPs for the remaining experiments. In an inflammatory environment, inflammatory factors such as IL-1 $\beta$  can lead to mitochondrial dysfunction, oxidative stress, and cellular pyroptosis, which severely impede disc repair [40]. In the present study, IL-1 $\beta$  stimulation caused cells to produce excessive ROS, which was confirmed using an oxidative stress probe (DCFH-DA) (Fig. 3H). In contrast, the fluorescence was significantly attenuated after incubation with the TMP NPs, and ROS fluorescence was further reduced as the TMP NPs concentrations increased. Semi-quantitative analysis confirmed the strong ROS-scavenging property of the NPs (Fig. 3J). We then quantified fluorescence using flow cytometry (Fig. 3G) and found that TMP NP concentrations greater than 100  $\mu\text{g}/\text{mL}$  exhibited drastically reduced fluorescence to almost background levels, indicating that TMP is highly effective for scavenging ROS. To verify the improvement in the active state of the organelle, based on the decrease in ROS, we observed changes in the mitochondrial membrane potential (Fig. 3I). The JC-1 assay revealed a noteworthy augmentation in green fluorescence following IL-1 $\beta$  intervention, which was likely linked to the reduction in mitochondrial membrane potential owing to the existence of JC-1 in its monomeric form. With the intake of NPs, the mitochondrial membrane potential fluorescence gradually changed from green to red, and JC-1 aggregated in the mitochondrial matrix to form a polymer [41], thus confirming that the NPs improved mitochondrial activity (Fig. 3K).

### 3.4. Characterization of the TMP@Alg-PBA/PVA hydrogel release platform

The high fluidity of nanosolutions used for disc injection therapy often poses a significant safety hazard [42]. Solutions injected into IVDs can flow to critical surrounding areas, such as the spinal cord, thereby posing a serious threat to life [43]. To avoid such risks, the preparation of effective NPs carriers is essential. That's why there is no need to validate the efficacy of nanosolutions without hydrogel against IVDD separately in subsequent experiments. In the clinical specimen results, nucleus pulposus tissue degeneration was disorganized and unevenly distributed. Therefore, the design of a microenvironmentally-responsive release platform that releases NPs locally in degenerated areas while remaining stable in healthy tissues, ultimately enables on-demand and efficient drug delivery, is paramount. Alg, PBA, and PVA were chosen to prepare the platform. Alg was conjugated to PBA through an amide bond, after which a borate bond with PVA was established, which was susceptible to disruption in the presence of ROS. To identify the most suitable Alg-PBA:PVA ratio, concentration gradients of 3%, 6%, and 9% for both components were used and combined in different proportions to monitor gel formation. The combination of 9% Alg-PBA and 6% PVA led to optimal hydrogel formation, whereas the other combinations led to the material remaining in liquid or viscous states (Fig. S6). We mixed TMP into PVA to form TMP@PVA, after which Alg-PBA was added and the rapid formation of a gel was achieved (Fig. 4A). The resulting gel was placed obliquely; it remained stable for a while, indicating successful gel formation.

An FTIR analysis revealed notable peaks at 1417  $\text{cm}^{-1}$  and 1304  $\text{cm}^{-1}$ , representing the O–C–O symmetry vibrations of the pyranose ring and C–C–H and O–C–H deformations, respectively. Additionally, peaks at 1350  $\text{cm}^{-1}$  and 1300  $\text{cm}^{-1}$  corresponded to B–O stretching vibrations. The inclusion of PBA led to a slight broadening of the pyranose ring peaks in the spectra, and a new peak at 711  $\text{cm}^{-1}$  signified the presence of C–H vibrations from aromatic hydrocarbons. These findings collectively confirmed the successful coupling of Alg with PBA via an amide bond. Furthermore, the absence of a peak at approximately 1340  $\text{cm}^{-1}$  in Alg-PBA/PVA, compared to that of Alg-PBA, suggested the successful preparation of Alg-PBA/PVA via the formation of borate bonds between the two components (Fig. 4B). Subsequent SEM analysis of the freeze-dried hydrogel revealed its loose porous structure and confirmed the successful loading of the TMP NPs (Fig. 4C). Furthermore, the EDS

analysis confirmed the uniform presence of carbon, oxygen, nitrogen, and manganese on the hydrogel surface, providing evidence of an even distribution of the TMP NPs across the platform (Fig. 4D).

The hydrogel exemplified in Fig. 4E exhibited excellent moldability, enabling the creation of an "IVDD" pattern. Fig. 4F offers evidence of the injectability of the hydrogel, thereby supporting the rationale for IVD injection therapy. Notably, rheological characterization revealed a distinctive shear-thinning behavior of the material, accompanied by a robust storage modulus ( $G'$ ) exceeding  $10^3$  Pa. Importantly, throughout the testing range,  $G'$  consistently eclipsed  $G''$ , further affirming the stability of the hydrogel (Fig. 4G). Fig. 4H shows that, at lower frequencies, the hydrogel experienced stress, which caused the extensive movement and deformation of the entangled molecular chains within the network structure and, consequently, a higher  $G''$  value was obtained. In contrast, the molecular chains lacked sufficient relaxation at higher frequencies, culminating in an elevated  $G'$ . IVD-injected hydrogel systems should have good self-healing properties to counteract long-term mechanical damage to the disc [44]. To evaluate the self-healing properties of the release platform, we physically separated it and observed that it healed within 15 min and reconnected seamlessly at the contact interface, emphasizing the capacity of the hydrogel to endure tensile stress (Fig. 4I).

Finally, in the hydrogel degradation test, rhodamine-B was released as the hydrogel degraded in 400  $\mu\text{M}$   $\text{H}_2\text{O}_2$ , diffused to approximately 50% of the solution after 12 h, and then to approximately 75% after 24 h. After 48 h, the hydrogel was almost completely degraded, and rhodamine-B was dispersed into the solution. In contrast, the appearance of the hydrogel in PBS changed only slightly, which highlighted the effective response of the hydrogel to ROS stimulation (Fig. 4J). In addition, we set up different gradients of hydrogen peroxide such as 0, 50, 100, and 200  $\mu\text{M}$  were used to observe the responsiveness of the platform (Fig. S7). The results showed that as the increase of hydrogen peroxide concentration, the degradation of the platform was accelerated, demonstrating a concentration-dependent relationship with hydrogen peroxide. Therefore, TMP NPs is more easily released to the site of degeneration through this platform. Fig. 4K shows the in vitro drug release from the TMP@Alg-PBA/PVA microenvironment-responsive release platform in different release media. The platform possessed a low cumulative NPs release rate in the absence of  $\text{H}_2\text{O}_2$  in the release medium, and the cumulative NPs release from the hydrogel was significantly increased following the addition of  $\text{H}_2\text{O}_2$ . The ROS responsiveness of the hydrogel occurred when the B–C bond was oxidized to phenol after the coordination of  $\text{H}_2\text{O}_2$  and boron atoms in the microenvironment. The borate bond was broken, disrupting the network structure of the hydrogel and enhancing the release of NPs (Fig. 4L). Overall, the characteristics of the release platform are promising for using in IVD injections.

### 3.5. Cellular uptake, lysosomal escape, and mitochondrial accumulation of TMP NPs

The efficiency of cellular uptake of NPs is crucial for efficiency of treatment. To monitor NPs uptake and distribution, the TMP NPs were attached to CY5 fluorescence and loaded into the hydrogels [45]. The uptake of the NPs gradually increased as the loading concentration increased (Fig. 5A). When the concentration of the NPs loaded into the hydrogel exceeded 200  $\mu\text{g}/\text{mL}$ , no significant increase in cellular uptake was observed. Before performing subsequent experiments, we needed to ensure that the release platform would not be toxic or negatively affect the cells. Therefore, the live and dead staining of the cells and the hemolysis experiment were performed. The TMP@Alg-PBA/PVA hydrogels loaded with 100  $\mu\text{g}/\text{mL}$  and 200  $\mu\text{g}/\text{mL}$  NPs exhibited great biocompatibility (Figs. S8 and 9); thus, these hydrogels were selected for the subsequent experiments. When the NPs concentration was constant, the fluorescence intensity of the NPs in the cells gradually increased as the co-culture duration increased (Fig. 5C). Semi-quantitative analysis

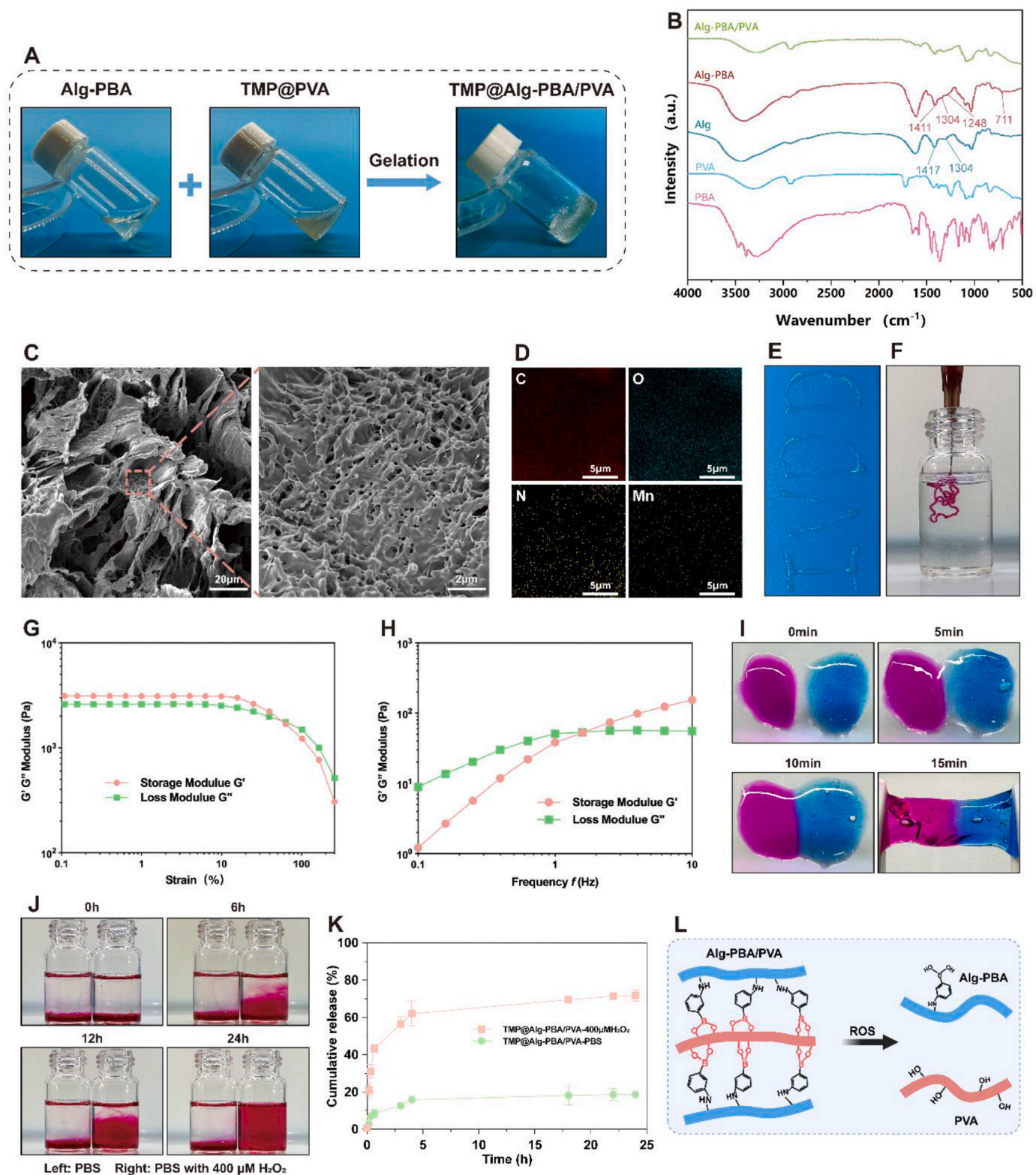


**Fig. 4.** Characterization of the TMP@Alg-PBA/PVA hydrogel release platform. **A)** Sol-gel transition of the TMP@Alg-PBA/PVA hydrogel. **B)** FTIR analyses of PBA, PVA, Alg, Alg-PBA, and Alg-PBA/PVA. **C)** SEM images of the hydrogel. **D)** EDS images of the hydrogel. **E, F)** Moldability and injectability of the hydrogel. **G)** Strain-dependent rheological behavior of the hydrogel. **H)** Frequency-dependent rheological behavior of the hydrogel. **I)** Self-healing property of the hydrogel (stained with rhodamine-B and methylene blue). **J)** ROS-responsive degradability of the hydrogel. **K)** *In vitro* release assay of the hydrogels (N = 3). **L)** Fracture mechanism of the Alg-PBA/PVA hydrogel network.

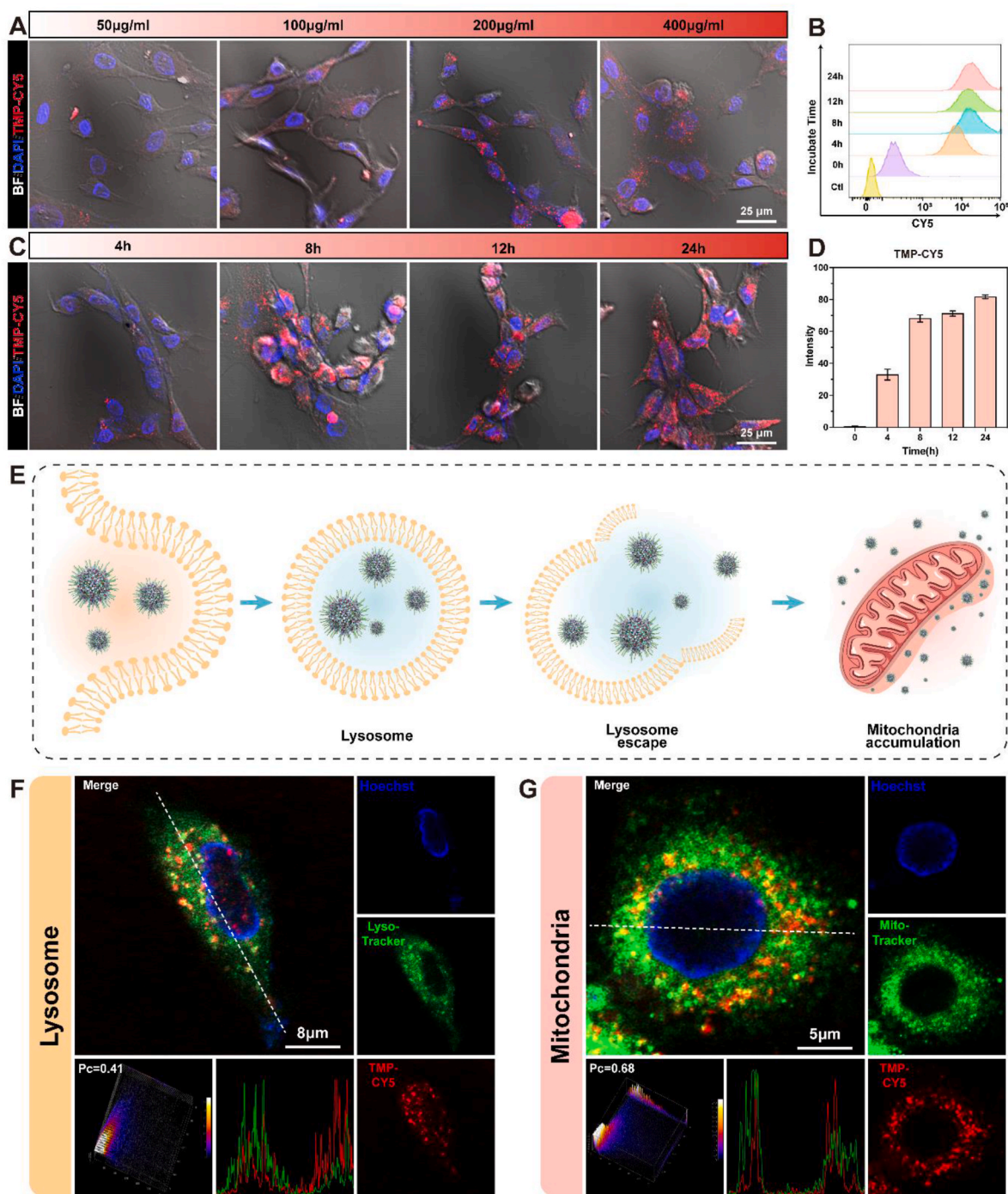


**Fig. 5.** Cellular uptake, lysosomal escape, and mitochondrial accumulation of TMP NPs. A, C) Confocal microscopy images of TMP-CY5 cellular uptake at different concentrations and durations. B) Flow cytometry analysis of TMP-CY5 uptake and retention in NPCs. D) Semi-quantification of TMP-CY5 cellular uptake ( $N = 4$ ). E) Schematic of TMP uptake. F) Co-localization of the NPs (red) with lysosomes (green). G) Confocal microscopy images of the co-localization of mitochondria (green) and NPs (red). Red: CY5-labeled TMP, green: lysosome or mitochondria, blue: nucleus, BF: bright field.

revealed that the fluorescence intensity rapidly increased to approximately 70% during the first 8 h, followed by a slow increase to 80% (Fig. 5D). The flow cytometry results showed the same trends (Fig. 5B). The TMP NPs therefore exhibited rapid uptake and prolonged retention in NPCs, making them suitable for immediate cell treatment and long-term protection.

Following cellular uptake, TMP NPs enter lysosomes through receptor interactions [46]. Lysosomes serve as crucial barriers that inhibit the intracellular functionality of NPs. We therefore investigated the

potential of NPs to evade lysosomes and access the cytoplasm. The results revealed successful NPs escape from lysosomes and release into the cytoplasm (Fig. 5F and S10). The subcellular location of NPs is also a key determinant of their therapeutic efficacy [46]. Mitochondria are the main sources of ROS and induce oxidative stress in cells [47]; thus, targeting mitochondria is crucial for effective ROS removal. TA is a polyphenolic compound that strongly binds to proteins via hydrophobic and hydrogen bonds [48]. Many studies have been conducted to utilize protein-binding TA for its therapeutic effects [49,50]. Recently, Mao

et al. found that TA can bind to the two most abundant proteins, voltage-dependent anion selective channel and translocase of the outer membrane, on the outer mitochondrial membrane and exert excellent mitochondria-targeting properties [19]. Given the substantial loading of TA NPs, we posited that TMP NPs similarly exhibit exceptional mitochondrial targeting capabilities. To evaluate the mitochondria-targeting capability of the TMP NPs, we incorporated CY5-labeled TMP into hydrogels co-cultured with NPCs. Mito-tracker fluorescent labeling was employed to visualize the mitochondria. There was a substantial overlap between the green fluorescent mitochondria and red fluorescent NPs, which resulted in the emission of yellow light (Fig. 5G and S11). A fluorescence co-localization analysis yielded a Pearson's correlation coefficient of approximately 0.65, indicating a significant positive relationship between the NPs and mitochondria. In summary, after being absorbed by cells, NPs can be released into the cytoplasm via lysosomal escape and then target the mitochondrial region to facilitate the more effective clearance of ROS by TMP (Fig. 5E).

### 3.6. Effects of the TMP@Alg-PBA/PVA hydrogel release platform on pyroptosis *in vitro*

The accumulation of ROS and mitochondrial toxicity can mediate cellular pyroptosis through multiple pathways, such as the ROS-mediated promotion of the inflammatory vesicle NLRP3/caspase-1/GSDMD signaling pathway [51–53]. Given the close relationship between ROS and cellular pyroptosis, we hypothesized that TMP@Alg-PBA/PVA may also inhibit pyroptosis. We therefore investigated the potential of the platform to impede cellular pyroptosis. IL-1 $\beta$ , a highly representative pro-inflammatory factor, induces NPCs pyroptosis [23]; therefore, we used a CCK-8 assay kit to quantify the impact of IL-1 $\beta$  on NPCs death. Cell viability decreased by over 30% at a concentration of 40 ng/mL IL-1 $\beta$  (Fig. S12). Therefore, we induced NPCs death using IL-1 $\beta$  at a concentration of 40 ng/mL. Fig. 6A presents a visual representation of the co-culture of the hydrogel with NPCs. To determine the ability of the TMP@Alg-PBA/PVA hydrogels to inhibit cell death, we first assessed cell viability. We performed a CCK-8 assay for each group, which showed that the cell activity of the treatment group was significantly improved compared to that of the Gel and Control groups in a concentration-dependent manner (Fig. 6B). To visualize the cell death status, PI staining experiments were performed; the number of dead cells was observed to be significantly higher in the Gel and Control groups than in the Blank group (Fig. 6C). Apoptosis may also have contributed to this phenomenon [54]. Therefore, we performed a western blot analysis of apoptosis-related proteins to understand the effects of TMP@Alg-PBA/PVA on apoptosis (Fig. S13). The results revealed that apoptosis-related protein expression rose after the addition of IL-1 $\beta$ . In contrast, protein expression was not significantly changed after incubation with TMP@Alg-PBA/PVA, suggesting that this platform played a limited role in reducing apoptosis. Therefore, we hypothesized that this platform may affect cellular pyroptosis.

Cell membrane rupture and cleavage represent key characteristics of cells undergoing pyroptosis, typically induced by the GSDMD-NT-mediated perforation of the cell membrane [55]. Consequently, direct observations of cell membrane rupture and the quantification of LDH released from the cytoplasm following rupture are crucial for evaluating pyroptosis [56]. The LDH detection kit revealed a significant increase in LDH levels in the Control and Gel groups. In contrast, the TMP@Alg-PBA/PVA group exhibited reduced LDH accumulation, indicating diminished cell membrane rupture (Fig. 6D). Additionally, SEM revealed a notable increase in the quantity of pores on the cell membrane surface in the IL-1 $\beta$  group, accompanied by globular protrusions on the fragmented cell membranes. In contrast, the cell morphology in the treatment and Blank groups exhibited elongation and robust cell membrane integrity (Fig. 6E). This observation implies that the platform potentially mitigates the aforementioned phenomena by inhibiting cellular pyroptosis. To observe the changes in intracellular

inflammation, we used RT-qPCR experiments and found that, at the gene level, the expression of IL-1 $\beta$  and TNF- $\alpha$  mRNA was significantly reduced in the treatment group compared to that in the other groups (Fig. 6F). At the protein level, we assessed the expression of classical proteins related to pyroptosis, such as NLRP3, caspase-1, and GSDMD, using immunofluorescence in each group (Fig. 6G) [56,57]. Compared to that in the Blank group, the expression of NLRP3 and caspase-1 significantly increased in both the Gel and Control groups, and GSDMD-N significantly accumulated in the cell membrane. This phenomenon was attenuated by TMP@Alg-PBA/PVA, further indicating that IL-1 $\beta$  induces cellular pyroptosis and demonstrating the anti-pyroptotic properties of the platform. The same conclusion was confirmed by the western blot analysis (Fig. 6H). The above results suggest that TMP@Alg-PBA/PVA effectively inhibits cell pyroptosis.

### 3.7. Underlying mechanism through which TMP@Alg-PBA/PVA suppresses pyroptosis

Although the anti-pyroptotic properties of the TMP@Alg-PBA/PVA hydrogel were verified, the specific intracellular mechanism remained unclear. To assess the changes in the gene expression in NPCs, we conducted high-throughput mRNA sequencing to analyze intracellular mRNA changes (Fig. 7A). Volcano plots displayed significant differences in gene expression, wherein 2967 DEGs were identified between the two groups ( $|\log_2FC| \geq 1$ ,  $P < 0.05$ ). When comparing the treatment group to the IL-1 $\beta$  group, 1472 genes were upregulated, and 1495 genes were downregulated (Fig. 7B). A GO analysis was also performed, with cellular components indicated in red, biological processes in blue, and molecular functions in green (Fig. 7C). We took the top-10 results from each category for the analysis. The DEGs were mainly associated with developmental processes, cellular responses to chemical stimuli, cell differentiation, ECM, collagen-containing extracellular space, protein or signaling pathway binding, and activation.

To identify the signaling pathways associated with the DEGs, we performed a KEGG pathway enrichment analysis, which revealed the downregulation of the TNF signaling pathway, IL-17 signaling pathway, cell cycle, and Toll-like receptor signaling pathway in the treatment group (Fig. 7D). The IL-17 signaling pathway was markedly inhibited (Fig. 7E). Recent studies have shown that the IL-17 signaling pathway promotes cellular pyroptosis through the extracellular signal-regulated kinase (ERK)1/2 pathway in sinonasal mucosa [58]. Thus, we performed a western blot assay to analyze the expression of key proteins in the IL-17-induced pyroptosis-related signaling pathway (Fig. 7F). The expression of the IL-17/ERK signaling pathway and downstream pyroptosis-related proteins was significantly attenuated after the addition of the IL-17 inhibitor. This study is the first to identify the role of the IL-17/ERK signaling pathway in promoting the onset of pyroptosis in IVDD. Subsequently, we found that the IL-17/ERK signaling pathway was significantly downregulated in the treatment group, which suggests that the treatment group likely exhibited inhibited cellular pyroptosis via the IL-17/ERK signaling pathway. In conclusion, the levels of IL-17A, MEK, pMEK, ERK, pERK, NLRP3, caspase-1, and GSDMD-NT proteins were elevated in the IL-1 $\beta$ -treated NPCs, and the addition of the inhibitor and TMP@Alg-PBA/PVA reversed these effects and attenuated the onset of cellular pyroptosis. TMP@Alg-PBA/PVA exerted the same effect as that of the IL-17A inhibitor. Collectively, these results suggest that TMP@Alg-PBA/PVA reduce cellular pyroptosis probably by suppressing the IL-17/ERK signaling pathway in NPCs, thus providing a new possible target for IVDD therapies.

### 3.8. Changes in the ECM after TMP@Alg-PBA/PVA treatment

The main features of IVDD are water molecule loss, ECM degradation, increased fibrosis, and resulting mechanical damage to the disc [1]. Current research suggests that reducing ROS accumulation and cellular pyroptosis reduces ECM degradation [59]. Trace amounts of divalent

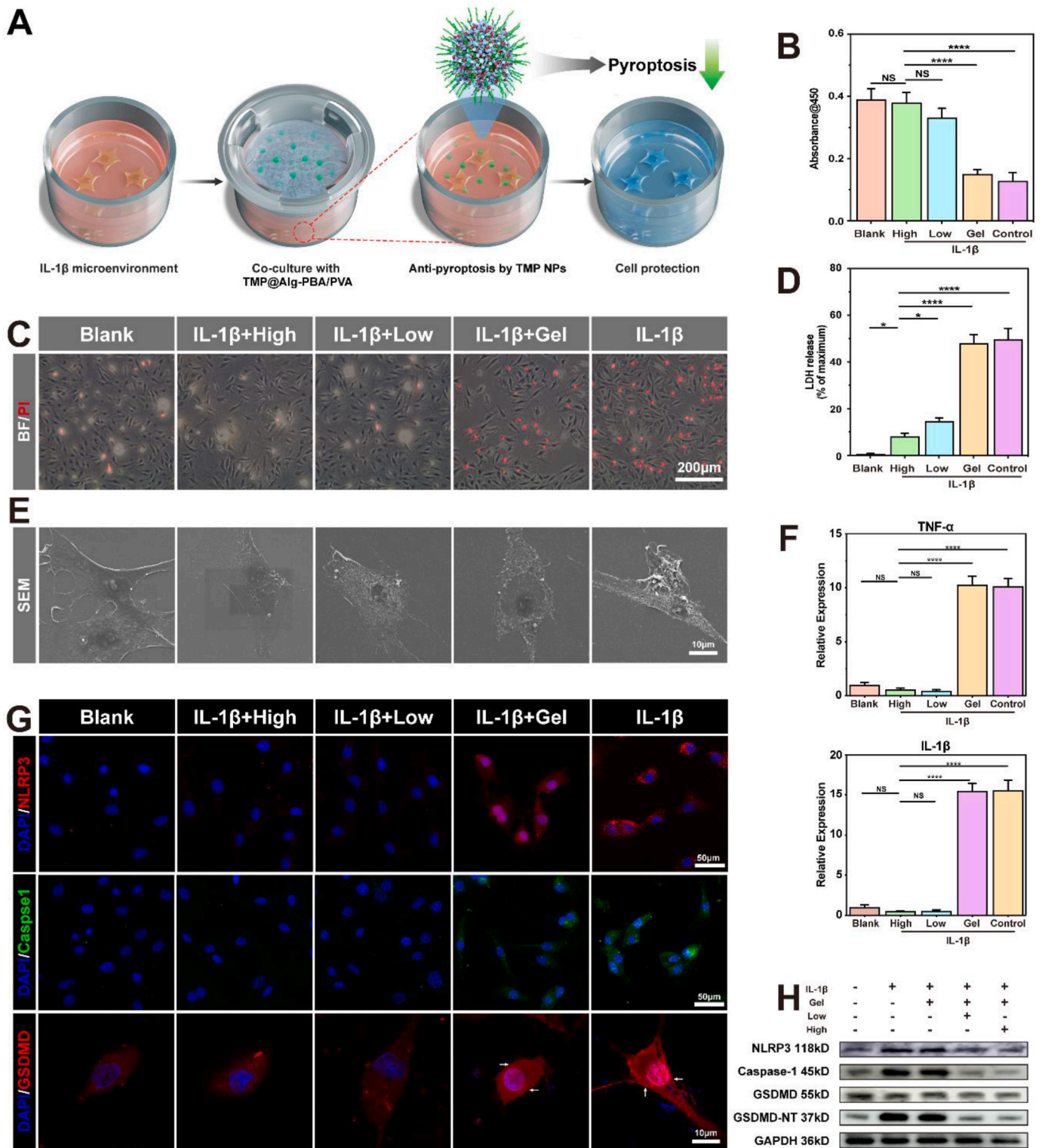


**Fig. 6.** Effects of TMP@Alg-PBA/PVA on pyroptosis. A) Schematic of the hydrogel-NPC co-culture system. B) CCK-8 assay to determine cell viability. C) NPCs survival detected using PI staining (red fluorescence, induced by propidium iodide, indicates dead cells). D) LDH released by NPCs. E) SEM images of the cell membrane. F) RT-qPCR analysis of IL-1 $\beta$  and TNF- $\alpha$  mRNA expression. G) Immunofluorescence images of the expression of NLRP3, caspase-1, and GSDMD in NPCs. H) Western blot images of NLRP3, caspase-1, GSDMD, and GSDMD-NT protein levels. High group: TMP@Alg-PBA/PVA hydrogel containing 200  $\mu$ g/mL TMP NPs; Low group: TMP@Alg-PBA/PVA hydrogel containing 100  $\mu$ g/m TMP NPs; Gel: Alg-PBA/PVA. \* $P$  < 0.05, \*\* $P$  < 0.01, \*\*\* $P$  < 0.001, \*\*\*\* $P$  < 0.0001 vs. High group. NS vs. High group, not significant. N = 4.

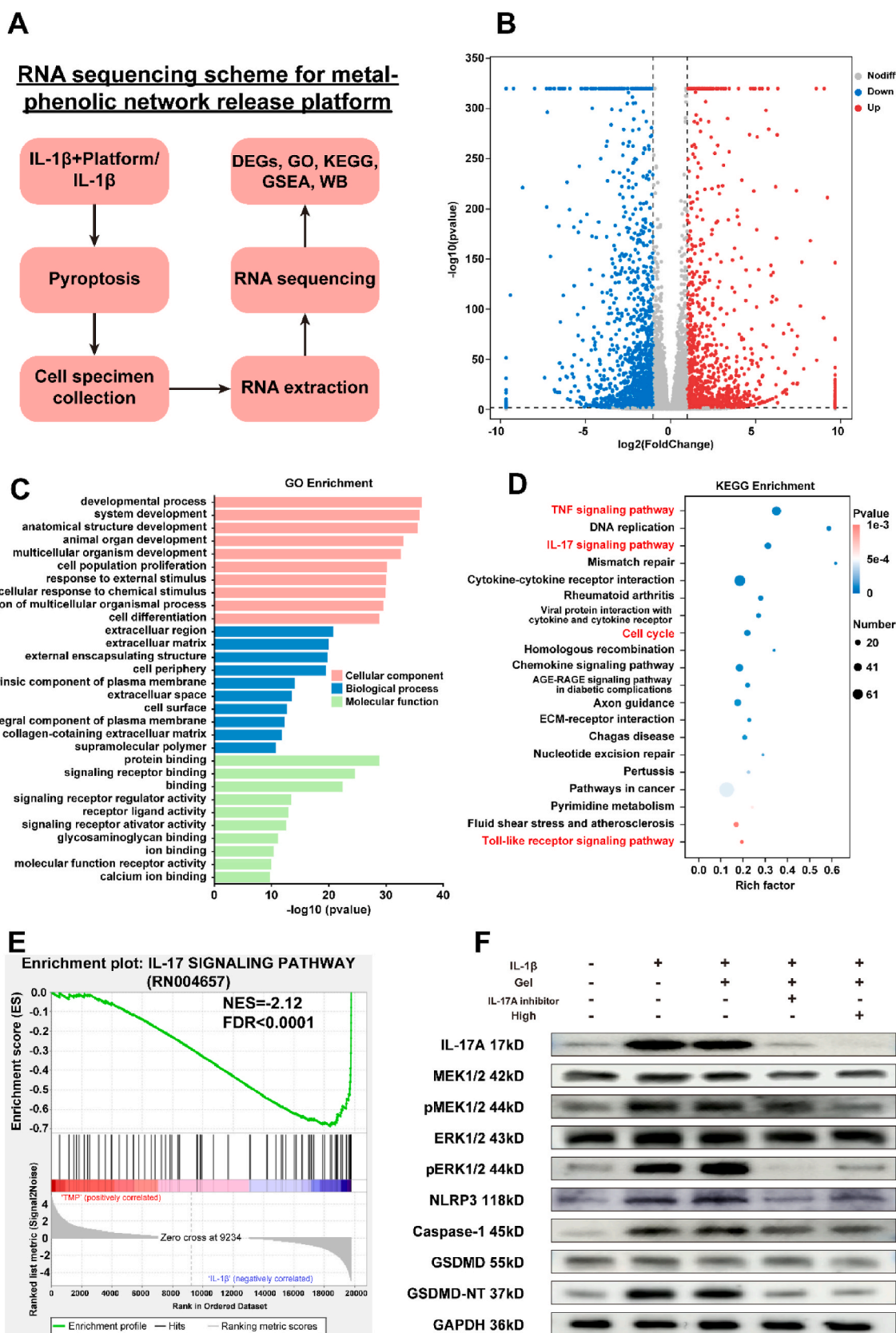


**Fig. 7.** Transcriptomic analyses. A) RNA sequencing scheme for metal-phenolic network release platform. B) Volcano plot of DEGs. Red dots indicate upregulated genes, and blue dots indicate downregulated genes. C) GO analysis showing the cellular components, biological processes and molecular functions of the DEGs. D) KEGG enrichment pathway analysis. E) GSEA showing the suppression of the IL-17 signaling pathway in the treatment group. F) Western blot analysis of proteins related to the IL-17/ERK pyroptosis signaling pathway.

Mn<sup>2+</sup> are thought to be essential for the activity of prolylase, an enzyme involved in the hydrolysis of proline and hydroxyproline, which are important components of collagen. The Mn<sup>2+</sup> released from this platform may provide a localized Mn<sup>2+</sup> environment for NPCs, thereby accelerating collagen recycling and promoting effective ECM remodeling [35]. Therefore, we inferred that this platform would reduce ECM degradation in an inflammatory environment. Aggrecan and Col-II are pivotal components of the nucleus pulposus ECM and serve as essential biomarkers for assessing ECM function [60]. Inflammatory factors such as IL-1 $\beta$  cause the low expression of both components [61]. We utilized IL-1 $\beta$  to stimulate NPCs and simulate the impact of an inflammatory environment on the ECM. Following the IL-1 $\beta$  treatment, there was a significant reduction in the fluorescence intensities of aggrecan and Col-II compared to those in the Blank group (Fig. 8A). This reduction

indicated that IL-1 $\beta$  severely impaired the ability of the NPCs to remodel the ECM. The fluorescence intensities of the two proteins remained relatively unchanged in the Gel group. However, the fluorescence intensities of aggrecan and Col-II increased in the High and Low groups, respectively. A similar conclusion was reached at the level of gene expression (Fig. 8B).

The gene expression of crucial biological enzymes that regulate the ECM was also explored [60]. The TMP@Alg-PBA/PVA treatment effectively reduced the expression of ECM degradation enzymes, namely, MMP-3, MMP-13, and ADAMTS-5, which had been elevated following the addition of IL-1 $\beta$ , bringing their levels closer to those in the Blank group (Fig. 8C). Moreover, the expression of TIMP-1, a tissue inhibitor of metalloproteinases preventing ECM degradation [62], exhibited a marked increase in the High and Low groups compared to that in the

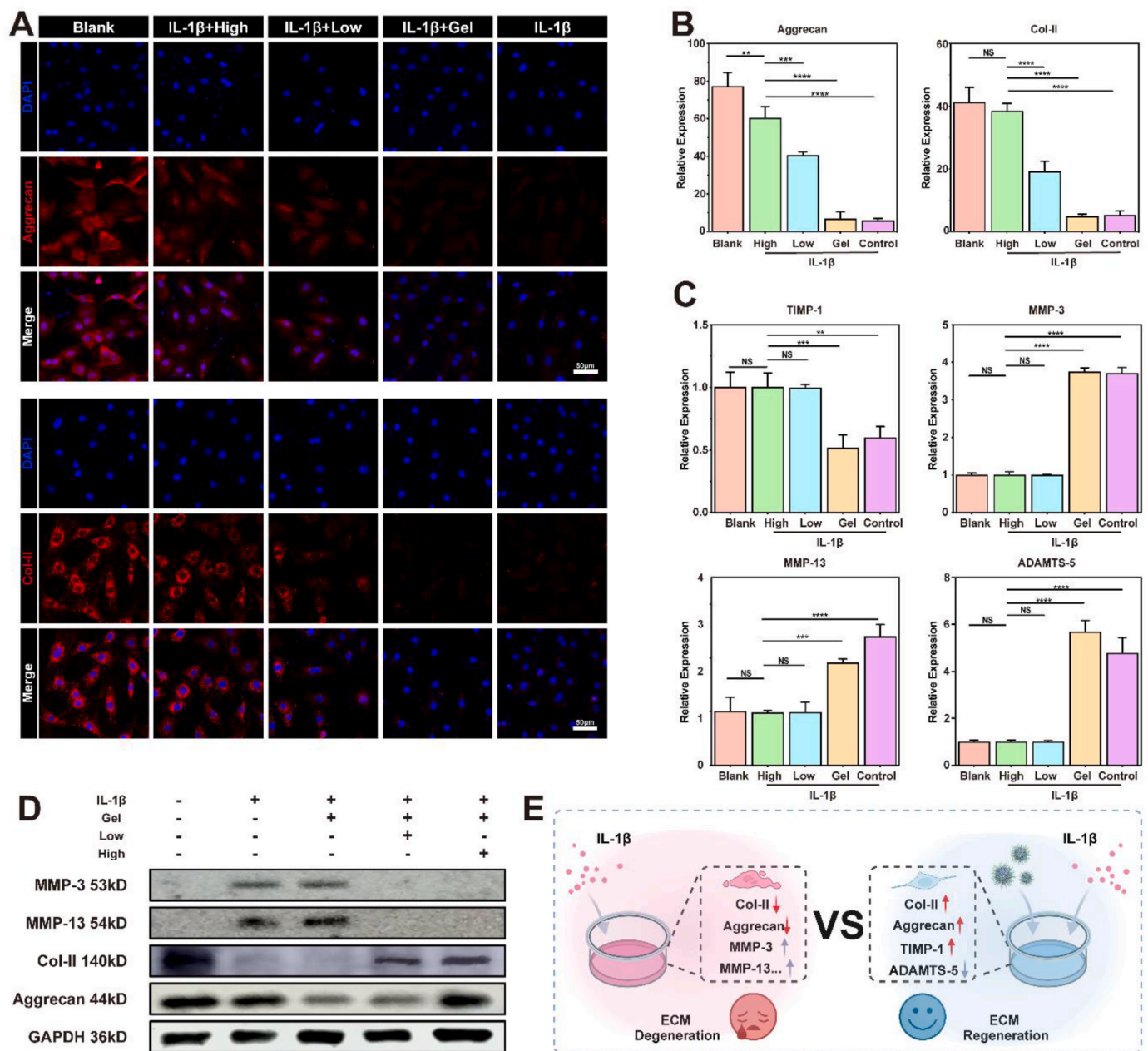


Fig. 8. Influence of TMP@Alg-PBA/PVA on ECM in an inflamed environment. A) Immunofluorescence analysis of aggrecan and Col-II expression in NPCs. B) RT-qPCR semi-quantitative analysis of aggrecan and Col-II mRNA levels. C) RT-qPCR results of the transcriptional profiles of the ECM-degrading enzymes MMP-3, MMP-13, ADAMTS-5, and TIMP-1. D) Western blotting detection of aggrecan, Col-II, MMP-3 and MMP-13 proteins in NPCs. E) Related changes before and after treatment. \*\* $P < 0.01$ , \*\*\* $P < 0.001$ , \*\*\*\* $P < 0.0001$ .; NS vs. High group, not significant. N = 4.

IL-1 $\beta$  group (Fig. 8C). To further confirm these findings, we performed western blotting to evaluate the protein expression levels of MMP-3, MMP-13, aggrecan and Col-II in NPCs across various intervention groups. As depicted in Fig. 8D, the results were consistent with the immunofluorescence data, revealing a significant reduction in the expression of aggrecan and Col-II in the IL-1 $\beta$  group compared to that in the Blank group. In addition, the High and Low group inhibited the expression of MMP-3 and MMP-13 proteins in the inflammatory environment, reducing the negative impact of ECM degradation. Notably, the Gel group failed to counteract the negative impact of IL-1 $\beta$ , whereas the High and Low groups showed an effective increase in the expression of aggrecan and Col-II. These results suggest that the TMP@Alg-PBA/PVA platform counteracts the detrimental effects of IL-1 $\beta$  on ECM, showing promise for IVD repair and regeneration (Fig. 8E).

### 3.9. Effects of TMP@Alg-PBA/PVA on an IL-1 $\beta$ -induced rat IVDD model

To assess the efficacy of TMP@Alg-PBA/PVA *in vivo*, we induced IVDD in rats by IL-1 $\beta$  and assessed the therapeutic effects of the hydrogel. To ensure that IL-1 $\beta$  could adequately induce disc

degeneration, we chose to intervene 3 days after the IL-1 $\beta$  injection [62]. We injected 10  $\mu$ L of the TMP@Alg-PBA/PVA release platform *in situ* in the IVDD rats (Fig. 9A) [63]. We then conducted imaging and histological analyses of rat tails after 4 and 8 weeks to assess IVD degeneration or regeneration. Before assessing the therapeutic effects, we conducted an *in vivo* toxicity study. After 4 weeks, HE staining revealed no significant organ damage, confirming the safety of the TMP@Alg-PBA/PVA platform (Fig. S14).

Subsequently, we focused on the effects of the IVDD treatment. Firstly, we visualized structural changes using radiography and MRI. For a quantitative assessment of the therapeutic effects, we calculated the changes in the DHI based on the radiographic results. As shown in Fig. 9B–D, and E, a significant decrease in DHI and a marked increase in the formation of osteophyte was observed in the PBS group compared to that in the Sham group. A significant decrease in DHI was also observed in the Gel group, suggesting that both the Gel and PBS failed to effectively attenuate IVDD. However, the decrease in the DHI slowed with the addition of hydrogel containing 200  $\mu$ g/mL of TMP NPs (High group) and hydrogel containing 100  $\mu$ g/mL of TMP NPs (Low group). The results of the High group were better than those of the Low group and similar to those of the Sham group, indicating that the low- and high-

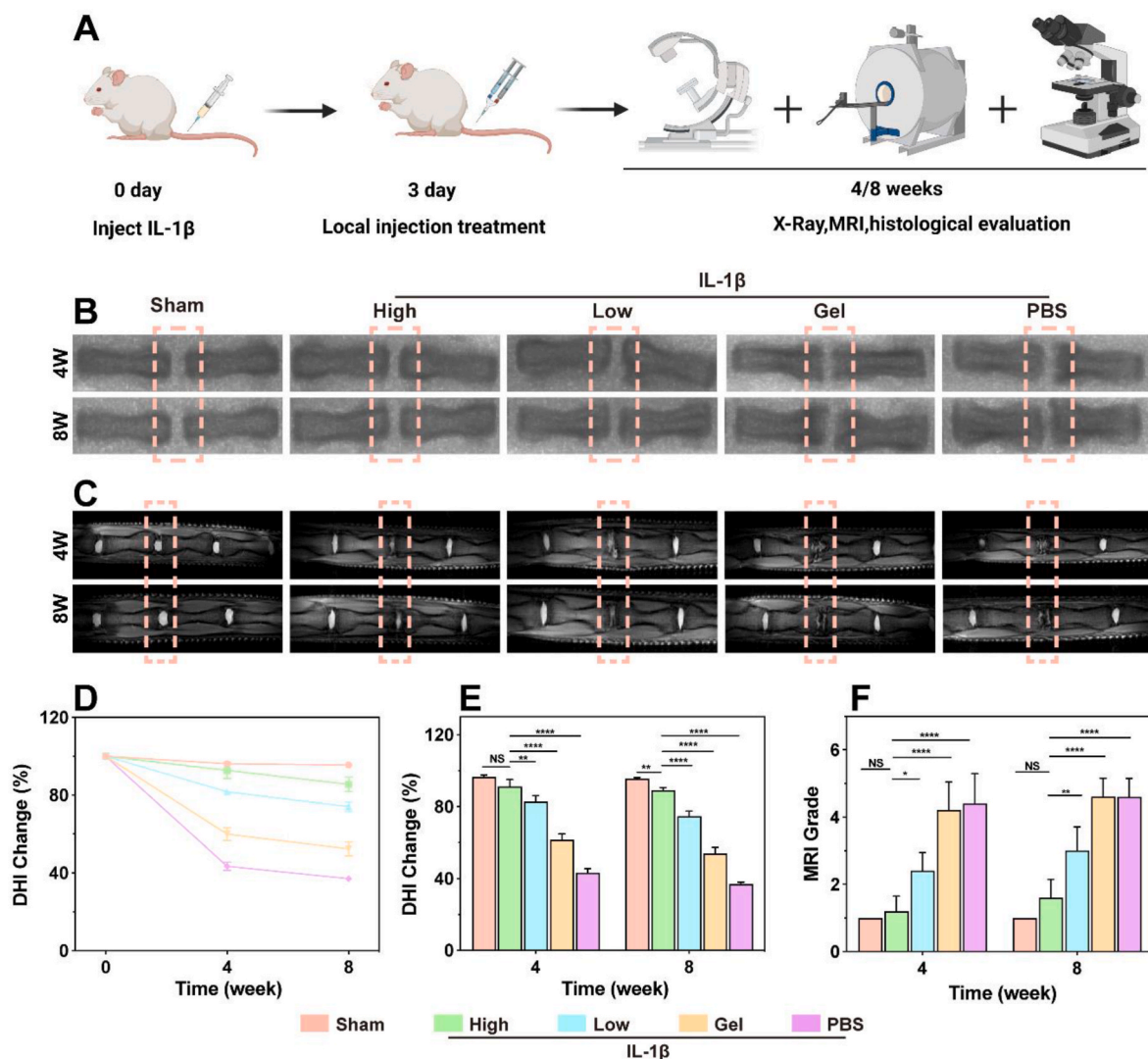


**Fig. 9.** Imaging evaluation of the animal experiments. A) Schematic of the *in vivo* experimental manipulation. B, C) X-ray and MR images of IVDD rat tails. D, E) Quantitative analysis of DHI changes after 4 and 8 weeks. F) Quantitative analysis of MRI grading changes after 4 and 8 weeks. High group: Alg-PBA/PVA containing 200  $\mu$ g/mL of TMP NPs, Low group: Alg-PBA/PVA containing 100  $\mu$ g/mL of TMP. \* $P$  < 0.05, \*\* $P$  < 0.01, \*\*\*\* $P$  < 0.0001 vs. Sham group. NS vs. Sham group, not significant.  $N$  = 5.

dose treatments were effective against IVDD. The nucleus pulposus tissue water content was measured based on T2-weighted MRI [64]. After 4 and 8 weeks, we noted a significant decrease in the disc signal in the PBS and Gel groups, respectively. The addition of TMP@Alg-PBA/PVA increased the T2-weighted signal, with the High group showing a higher signal than that of the Low group, illustrating the increased water content of the nucleus pulposus tissue and emphasizing the critical role of TMP@Alg-PBA/PVA in treating IVDD (Fig. 9C). The MRI grading

changes further confirmed these findings (Fig. 9F).

### 3.10. Histological staining and immunohistochemistry

To observe the histological changes in IVDs, we sectioned and stained the degenerate tissues from the IVDD rat tails. HE staining revealed that, compared to the Sham group, the PBS and Gel groups exhibited a significant loss of typical tissue structure, nucleus pulposus

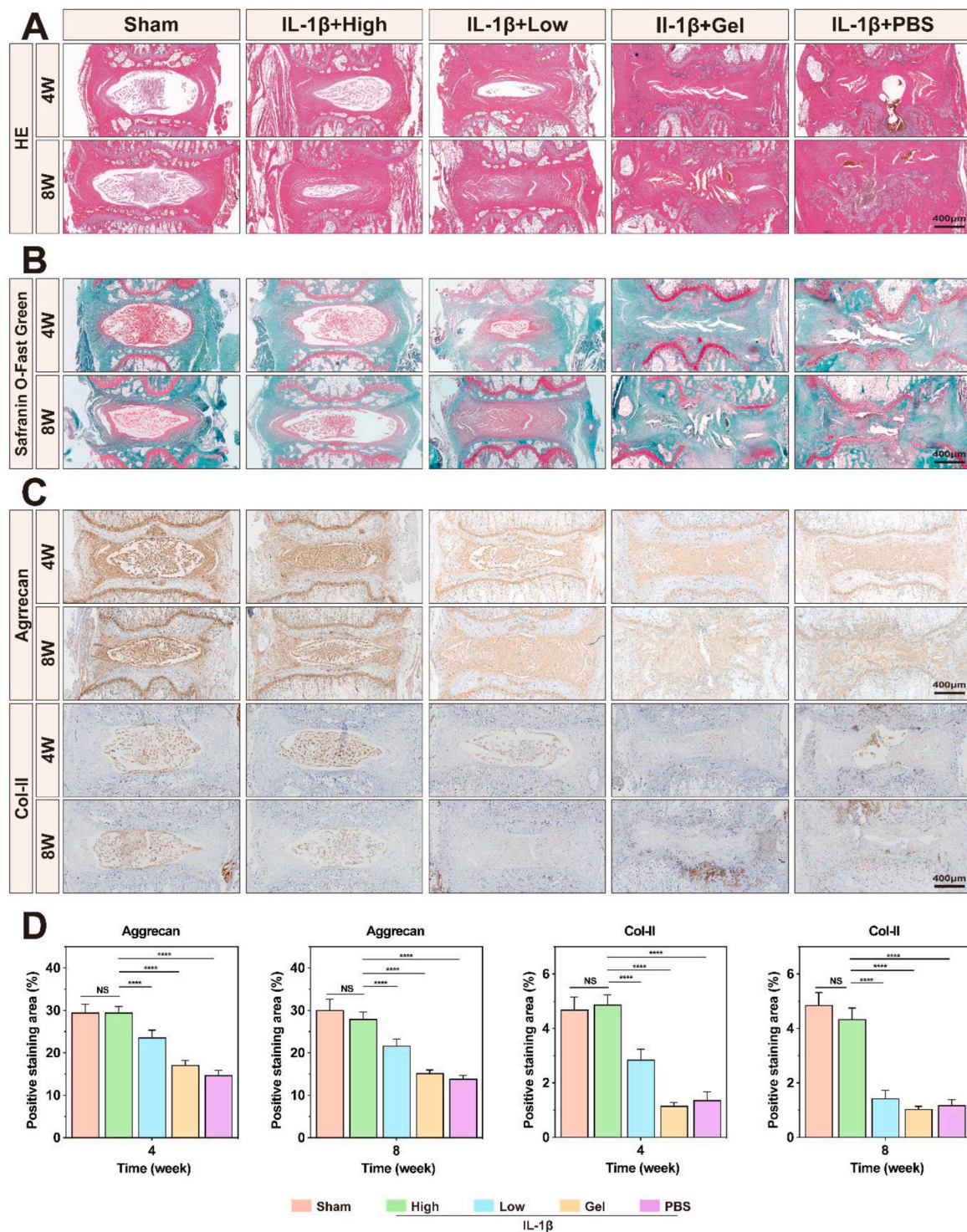


**Fig. 10.** Histological and immunohistochemical analyses of IVDD rat tails. A) HE and B) Safranin O-Fast Green staining show histological changes. C) Immunohistochemical staining for aggrecan and Col-II. D) Semi-quantitative analysis of immunohistochemical staining for aggrecan and Col-II. \* $P < 0.05$ , \*\* $P < 0.01$ , \*\*\*\* $P < 0.0001$  vs. High group. NS vs. High group, not significant.  $N = 5$ .

tissue atrophy, and significant fibrous tissue infiltration. Conversely, the High and Low groups displayed clear tissue boundaries without prominent fibrosis and better maintenance of the cartilage endplate morphology (Fig. 10A). Similarly, Safranin O-Fast Green staining indicated a substantial reduction in the presence of the nucleus pulposus (red) within the intervertebral space in both the PBS and Gel groups following IL-1 $\beta$  intervention, in contrast to that in the Sham group. This reduction was concomitant with pronounced fibrosis (green) and the notable destruction of the cartilage endplate. Conversely, the High and Low groups mitigated this phenomenon, preserving a distinct boundary between the annulus fibrosus and nucleus pulposus (Fig. 10B). These preliminary results demonstrate the vital role of the hydrogel platform in treating IVDD *in vivo*.

To assess the effectiveness of the TMP@Alg-PBA/PVA platform in mitigating ECM degradation *in vivo*, we used immunohistochemistry to evaluate the expression of proteins related to the ECM within IVD tissues. Following the IL-1 $\beta$  intervention, the expression levels of Col-II and aggrecan significantly decreased in the PBS group compared to those in the Sham group. The Gel group exhibited no significant impact on the expression of these proteins compared to that in the PBS group. In contrast, the High and Low groups showed a significant increase in the expression of the proteins. Importantly, the expression levels of the proteins in the High and Low groups did not differ significantly from those in the Sham group (Fig. 10C). These findings were confirmed by semi-quantitative analysis, which underscored the effectiveness of the hydrogel platform in counteracting ECM degradation and maintaining the IVD water content (Fig. 10D).

### 3.11. Mechanism of action of TMP@Alg-PBA/PVA in the treatment of IVDD *in vivo*

To assess the potential of TMP@Alg-PBA/PVA in attenuating IVDD through the mitigation of cellular pyroptosis, we conducted immunofluorescence staining on IVD nucleus pulposus tissue. Caspase-1 was labeled with red fluorescence, and GSDMD was labeled with green fluorescence (Fig. 11A). In the Sham and High groups, the caspase-1 and GSDMD proteins were essentially unexpressed, revealing only nuclear coloration. The Low group exhibited a marginal increase in red and green fluorescence, whereas both fluorescence signals were significantly augmented in the Gel and PBS groups, indicative of heightened cellular pyroptosis in these groups. Fluorescence semi-quantification revealed a concentration-dependent feature of the anti-pyroptotic effect, with the High group featuring substantial TMP loading and superior therapeutic effects (Fig. 11B and C). Additionally, the Gel and PBS groups exhibited a time-dependent increase in the expression of pyroptosis-related proteins. In summary, these observations elucidate that the TMP@Alg-PBA/PVA release platform can decelerate the progression of IVDD by mitigating pyroptosis.

## 4. Conclusions

In this study, we developed a multifunctional and microenvironment-responsive metal-phenolic network release platform (TMP@Alg-PBA/PVA) loaded with TMP NPs that are released on demand in response to ROS. The platform is therefore highly suitable for IVDD injection therapy. *In vitro* studies demonstrated that NPs released from the platform can target the mitochondria to efficiently scavenge ROS, reduce cellular cell pyroptosis, and impede ECM degradation. The

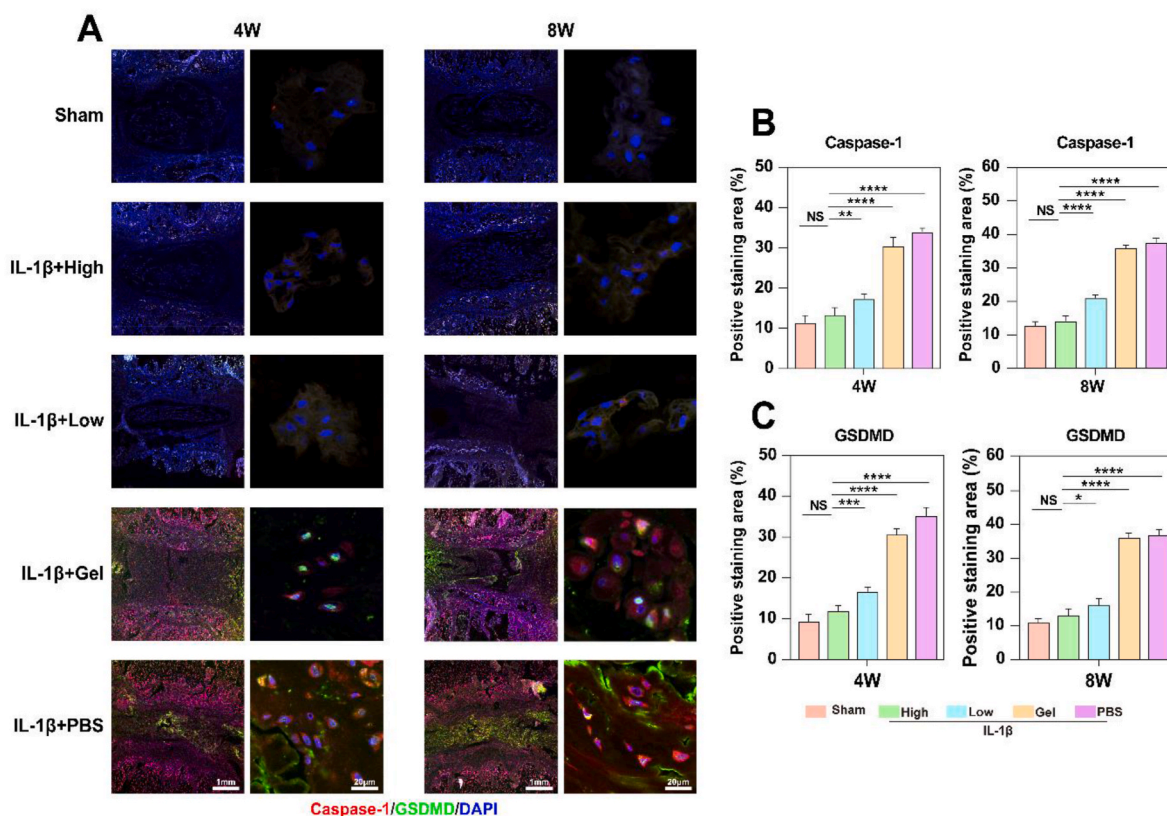


**Fig. 11.** Molecular mechanism underlying TMP-rescued IVDD in rats. A) Immunofluorescence staining results of rat IVD nucleus pulposus tissues under different intervention conditions and times. Nucleus in blue, GSDMD in green, and caspase-1 in red. B) Semi-quantitative analysis of immunofluorescence staining for caspase-1. C) Semi-quantitative analysis of immunofluorescence staining for GSDMD. \* $P < 0.05$ , \*\* $P < 0.01$ , \*\*\* $P < 0.001$ , \*\*\*\* $P < 0.0001$  vs. High group. NS vs. High group, not significant.  $N = 5$ .

proposed platform was biocompatible *in vivo*, inhibited the progression of IVDD, prevented cellular pyroptosis, and increased the water content in the IVD. Fundamentally, this platform provides an excellent approach for inhibiting pyroptosis in IVDD therapy, likely through the inhibition of the IL-17/ERK signaling pathway. Although several nanohydrogel platforms for scavenging ROS, suppressing pyroptosis, and reducing ECM degeneration have been reported [59,65], the hydrogel platform developed in the present study can be released on demand, efficiently utilizes NPs, and acts multilaterally. Overall, TMP@Alg-PBA/PVA has therapeutic potential for the treatment of IVDD and warrants further systematic preclinical studies. The identification of the IL-17/ERK signaling pathway as a molecular factor underlying the effects of the platform on IVDD further presents a potential target for treating pyroptosis.

#### CRedit authorship contribution statement

**Hao Zhou:** Conceptualization, Methodology, Validation, Formal analysis, Writing - Original Draft. **Jinpeng He:** Conceptualization, Methodology, Validation, Visualization, Writing - Original Draft. **Renfeng Liu:** Methodology. **Jun Cheng:** Methodology. **Yuhao Yuan:** Methodology. **Wanpu Mao:** Resources. **Jun Zhou:** Resources. **Honghui He:** Writing - Review & Editing. **Qianqi Liu:** Writing - Review & Editing. **Wei Tan:** Conceptualization, Funding acquisition. **Cijun Shuai:** Conceptualization, Writing - Review & Editing. **Youwen Deng:** Conceptualization, Writing - Review & Editing, Supervision, Project administration, Funding acquisition.

#### Ethics approval and consent to participate

The ethics review committee of the Affiliated Nanhua Hospital, University of South China, approved the clinical study protocol (2023-KY-61). The ethics review committee of the Department of Animal Experimentation, Central South University, approved the animal experiment protocol (CSU-2023-0436).

#### Declaration of competing interest

The authors declared that they have no known competing financial interests or personal relationships that could have appeared to influence the work reported in this paper.

#### Acknowledgements

This work was financially supported by the Key Projects of Hunan Provincial Science and Technology Department, China (2021RC4057), Key R&D Program of Hunan Provincial Science and Technology Department, China (2023SK2044), Natural Science Foundation of Hunan Province, China (2023JJ40906), Natural Science Foundation of Changsha, China (kq2208364). We would like to thank all colleagues who participated in this study for their outstanding contributions. In addition, we would like to thank Prof. Minhuan Lan and Prof. Pei Feng from Central South University for guiding our experimental content, and Prof. Wenjing Yang from Jiangxi University of Science and Technology for her help in revising the article, and Prof. Hui Wei from Nanjing University for help in modifying figures. Finally, thanks to Tao He, Lanmiao Ma, Yiting Chen, Di Wu, Bo Wang, Boyu Pan, Qizhi Fan and Hao Ning from Central South University, China for their notable support.

#### Appendix A. Supplementary data

Supplementary data to this article can be found online at <https://doi.org/10.1016/j.bioactmat.2024.02.036>.

#### References

- [1] Y. Li, H. Zhang, D. Zhu, F. Yang, Z. Wang, Z. Wei, Z. Yang, J. Jia, X. Kang, Notochordal cells: a potential therapeutic option for intervertebral disc degeneration, *Cell Prolif.* (2023) e13541, <https://doi.org/10.1111/cpr.13541>.
- [2] R.A. Deyo, J.D. Loeser, S.J. Bigos, Herniated lumbar intervertebral disk, *Ann. Intern. Med.* 112 (8) (1990) 598–603, <https://doi.org/10.7326/0003-4819-112-8-598>.
- [3] C. Findlay, S. Ayis, A.K. Demetriades, Total disc replacement versus anterior cervical discectomy and fusion: a systematic review with meta-analysis of data from a total of 3160 patients across 14 randomized controlled trials with both short- and medium- to long-term outcomes, *Bone Joint Lett. J* 100-b (8) (2018) 991–1001, <https://doi.org/10.1302/0301-620x.100b8.Bjj-2018-0120.R1>.
- [4] Y. Wang, H. Cheng, T. Wang, K. Zhang, Y. Zhang, X. Kang, Oxidative stress in intervertebral disc degeneration: molecular mechanisms, pathogenesis and treatment, *Cell Prolif.* 56 (9) (2023) e13448, <https://doi.org/10.1111/cpr.13448>.
- [5] T. Zhang, Y. Wang, R. Li, J. Xin, Z. Zheng, X. Zhang, C. Xiao, S. Zhang, ROS-responsive magnesium-containing microspheres for antioxidative treatment of intervertebral disc degeneration, *Acta Biomater.* 158 (2023) 475–492, <https://doi.org/10.1016/j.actbio.2023.01.020>.
- [6] C. Yu, D. Li, C. Wang, K. Xia, J. Wang, X. Zhou, L. Ying, J. Shu, X. Huang, H. Xu, et al., Injectable kartogenin and apocynin loaded micelle enhances the alleviation of intervertebral disc degeneration by adipose-derived stem cell, *Bioact. Mater.* 6 (10) (2021) 3568–3579, <https://doi.org/10.1016/j.bioactmat.2021.03.018>.
- [7] Y. Wang, M. Che, J. Xin, Z. Zheng, J. Li, S. Zhang, The role of IL-1 $\beta$  and TNF- $\alpha$  in intervertebral disc degeneration, *Biomed. Pharmacother.* 131 (2020) 110660, <https://doi.org/10.1016/j.biopha.2020.110660>.
- [8] Z. Li, S. Ji, M.L. Jiang, Y. Xu, C.J. Zhang, The regulation and modification of GSDMD signaling in diseases, *Front. Immunol.* 13 (2022) 893912, <https://doi.org/10.3389/fimmu.2022.893912>.
- [9] H. Liang, R. Luo, G. Li, W. Zhang, Y. Song, C. Yang, The proteolysis of ECM in intervertebral disc degeneration, *Int. J. Mol. Sci.* 23 (3) (2022), <https://doi.org/10.3390/ijms23031715>.
- [10] M.J. Kibble, M. Domingos, J.A. Hoyland, S.M. Richardson, Importance of matrix cues on intervertebral disc development, degeneration, and regeneration, *Int. J. Mol. Sci.* 23 (13) (2022), <https://doi.org/10.3390/ijms23136915>.
- [11] F. Hecht, M. Zocchi, F. Alimohammadi, I.S. Harris, Regulation of antioxidants in cancer, *Mol. Cell* (2023), <https://doi.org/10.1016/j.molcel.2023.11.001>.
- [12] W. Bao, H. Xing, S. Cao, X. Long, H. Liu, J. Ma, F. Guo, Z. Deng, X. Liu, Neutrophils restrain sepsis associated coagulopathy via extracellular vesicles carrying superoxide dismutase 2 in a murine model of lipopolysaccharide induced sepsis, *Nat. Commun.* 13 (1) (2022) 4583, <https://doi.org/10.1038/s41467-022-32325-w>.
- [13] C. Zhao, J. Chen, J. Ye, Z. Li, L. Su, J. Wang, Y. Zhang, J. Chen, H. Yang, J. Shi, J. Song, Structural transformative antioxidants for dual-responsive anti-inflammatory delivery and photoacoustic inflammation imaging, *Angew Chem. Int. Ed. Engl.* 60 (26) (2021) 14458–14466, <https://doi.org/10.1002/anie.202100873>.
- [14] Z. Li, F. Cai, J. Tang, Y. Xu, K. Guo, Z. Xu, Y. Feng, K. Xi, Y. Gu, L. Chen, Oxygen metabolism-balanced engineered hydrogel microspheres promote the regeneration of the nucleus pulposus by inhibiting acid-sensitive complexes, *Bioact. Mater.* 24 (2023) 346–360, <https://doi.org/10.1016/j.bioactmat.2022.12.025>.
- [15] J. Morla-Folch, A. Ranzenigo, Z.A. Fayad, A.J.P. Teunissen, Nanotherapeutic heterogeneity: sources, effects, and solutions, *Small* (2023) e2307502, <https://doi.org/10.1002/smll.202307502>.
- [16] K. Nasiri, S.M. Masoumi, S. Amini, M. Goudarzi, S.M. Tafreshi, A. Bagheri, S. Yasamineh, M. Alwan, M.T.C. Arellano, O. Gholizadeh, Recent advances in metal nanoparticles to treat periodontitis, *J. Nanobiotechnol.* 21 (1) (2023) 283, <https://doi.org/10.1186/s12951-023-02042-7>.
- [17] Z. Li, Y. Feng, S. Zhang, T. Li, H. Li, D. Wang, K. Hao, C. He, H. Tian, X. Chen, A multifunctional nanoparticle mitigating cytokine storm by scavenging multiple inflammatory mediators of sepsis, *ACS Nano* 17 (9) (2023) 8551–8563, <https://doi.org/10.1021/acsnano.3c00906>.
- [18] J. Ousingasawat, P. Wanitchakool, R. Schreiber, K. Kunzelmann, Contribution of TMEM16F to pyroptotic cell death, *Cell Death Dis.* 9 (3) (2018) 300, <https://doi.org/10.1038/s41419-018-0373-8>.
- [19] J. Zhang, B. Gao, B. Ye, Z. Sun, Z. Qian, L. Yu, Y. Bi, L. Ma, Y. Ding, Y. Du, et al., Mitochondrial-targeted delivery of polyphenol-mediated antioxidases complexes against pyroptosis and inflammatory diseases, *Adv. Mater.* 35 (11) (2023) e2208571, <https://doi.org/10.1002/adma.202208571>.
- [20] H. Zhang, H. Hu, Y. Dai, L. Xin, Q. Pang, S. Zhang, L. Ma, A conductive multifunctional hydrogel dressing with the synergistic effect of ROS-scavenging and electroactivity for the treatment and sensing of chronic diabetic wounds, *Acta Biomater.* 167 (2023) 348–360, <https://doi.org/10.1016/j.actbio.2023.05.045>.
- [21] L. Feng, L. Wang, Y. Ma, W. Duan, S. Martin-Saldaña, Y. Zhu, X. Zhang, B. Zhu, C. Li, S. Hu, et al., Engineering self-healing adhesive hydrogels with antioxidant properties for intrauterine adhesion prevention, *Bioact. Mater.* 27 (2023) 82–97, <https://doi.org/10.1016/j.bioactmat.2023.03.013>.
- [22] J. Rumpf, R. Burger, M. Schulze, Statistical evaluation of DPPH, ABTS, FRAP, and Folin-Ciocalteu assays to assess the antioxidant capacity of lignins, *Int. J. Biol. Macromol.* 233 (2023) 123470, <https://doi.org/10.1016/j.ijbiomac.2023.123470>.
- [23] H. Li, X. Wang, H. Pan, C. Xiao, C. Wang, S. Guo, L. Long, H. Shi, H. Chen, S. Li, The mechanisms and functions of IL-1 $\beta$  in intervertebral disc degeneration, *Exp. Gerontol.* 177 (2023) 112181, <https://doi.org/10.1016/j.exger.2023.112181>.
- [24] Z. Ma, P. Tang, W. Dong, Y. Lu, B. Tan, N. Zhou, J. Hao, J. Shen, Z. Hu, SIRT1 alleviates IL-1 $\beta$  induced nucleus pulposus cells pyroptosis via mitophagy in

- intervertebral disc degeneration, *Int. Immunopharm.* 107 (2022) 108671, <https://doi.org/10.1016/j.intimp.2022.108671>.
- [25] X. Yang, Y. Wu, M. Zhang, L. Zhang, T. Zhao, W. Qian, M. Zhu, X. Wang, Q. Zhang, J. Sun, L. Dong, Piceatannol protects against age-related hearing loss by inhibiting cellular pyroptosis and inflammation through regulated Caspase11-GSDMD pathway, *Biomed. Pharmacother.* 163 (2023) 114704, <https://doi.org/10.1016/j.biopha.2023.114704>.
- [26] J. Zhou, J. Qiu, Y. Song, T. Liang, S. Liu, C. Ren, X. Song, L. Cui, Y. Sun, Pyroptosis and degenerative diseases of the elderly, *Cell Death Dis.* 14 (2) (2023) 94, <https://doi.org/10.1038/s41419-023-05634-1>.
- [27] Y. Zheng, A. Baidya, N. Annabi, Molecular design of an ultra-strong tissue adhesive hydrogel with tunable multifunctionality, *Bioact. Mater.* 29 (2023) 214–229, <https://doi.org/10.1016/j.bioactmat.2023.06.007>.
- [28] Q. Guo, D. Zhu, Y. Wang, Z. Miao, Z. Chen, Z. Lin, J. Lin, C. Huang, L. Pan, L. Wang, et al., Targeting STING attenuates ROS induced intervertebral disc degeneration, *Osteoarthritis Cartilage* 29 (8) (2021) 1213–1224, <https://doi.org/10.1016/j.joca.2021.04.017>.
- [29] X. Jin, Z. Ou, G. Zhang, R. Shi, J. Yang, W. Liu, G. Luo, J. Deng, W. Wang, A CO-mediated photothermal therapy to kill drug-resistant bacteria and minimize thermal injury for infected diabetic wound healing, *Biomater. Sci.* 11 (18) (2023) 6236–6251, <https://doi.org/10.1039/d3bm00774j>.
- [30] Y. Feng, G. Wang, W. Li, J. Tang, Y. Zeng, X. Liu, D. Tang, Block-polymer-restricted sub-nanometer Pt nanoclusters nanozyme-enhanced immunoassay for monitoring of cardiac troponin I, *Anal. Chem.* 95 (38) (2023) 14494–14501, <https://doi.org/10.1021/acs.analchem.3c03249>.
- [31] W. Nie, A. Jiang, X. Ou, J. Zhou, Z. Li, C. Liang, L.L. Huang, G. Wu, H.Y. Xie, Metal-polyphenol "prison" attenuated bacterial outer membrane vesicle for chemodynamics promoted in situ tumor vaccines, *Biomaterials* 304 (2023) 122396, <https://doi.org/10.1016/j.biomaterials.2023.122396>.
- [32] X. Li, Y. Liu, X. Qi, S. Xiao, Z. Xu, Z. Yuan, Q. Liu, H. Li, S. Ma, T. Liu, et al., Sensitive activatable nanopores for real-time ratiometric magnetic resonance imaging of reactive oxygen species and ameliorating inflammation in vivo, *Adv. Mater.* 34 (19) (2022) e2109004, <https://doi.org/10.1002/adma.202109004>.
- [33] Y. Feng, G. Wang, W. Li, J. Yan, X. Yu, H. Tian, B. Li, Y. Dai, PhotoPyro-induced cGAS-STING pathway activation enhanced anti-melanoma immunotherapy via a manganese-coordinated nanomedicine, *Adv. Healthcare Mater.* (2023) e2302811, <https://doi.org/10.1002/adhm.202302811>.
- [34] T. Liu, B. Xiao, F. Xiang, J. Tan, Z. Chen, X. Zhang, C. Wu, Z. Mao, G. Luo, X. Chen, J. Deng, Ultrasmall copper-based nanoparticles for reactive oxygen species scavenging and alleviation of inflammation related diseases, *Nat. Commun.* 11 (1) (2020) 2788, <https://doi.org/10.1038/s41467-020-16544-7>.
- [35] B.M. Conley, L. Yang, B. Bhujel, J. Luo, I. Han, K.B. Lee, Development of a nanohybrid peptide hydrogel for enhanced intervertebral disc repair and regeneration, *ACS Nano* 17 (4) (2023) 3750–3764, <https://doi.org/10.1021/acsnano.2c11441>.
- [36] J. Yao, Y. Cheng, M. Zhou, S. Zhao, S. Lin, X. Wang, J. Wu, S. Li, H. Wei, ROS scavenging Mn(3)O(4) nanozymes for in vivo anti-inflammation, *Chem. Sci.* 9 (11) (2018) 2927–2933, <https://doi.org/10.1039/c7sc05476a>.
- [37] B.O. Milhoj, S.P. Sauer, Insight into the mechanism of the initial reaction of an OH radical with DNA/RNA nucleobases: a computational investigation of radiation damage, *Chemistry* 21 (49) (2015) 17786–17799, <https://doi.org/10.1002/chem.201503107>.
- [38] T.P. Ribeiro, C. Fernandes, K.V. Melo, S.S. Ferreira, J.A. Lessa, R.W. Franco, G. Schenk, M.D. Pereira, A. Horn Jr., Iron, copper, and manganese complexes with in vitro superoxide dismutase and/or catalase activities that keep *Saccharomyces cerevisiae* cells alive under severe oxidative stress, *Free Radic. Biol. Med.* 80 (2015) 67–76, <https://doi.org/10.1016/j.freeradbiomed.2014.12.005>.
- [39] Y. Peng, D. He, X. Ge, Y. Lu, Y. Chai, Y. Zhang, Z. Mao, G. Luo, J. Deng, Y. Zhang, Construction of heparin-based hydrogel incorporated with Cu5.4O ultrasmall nanozymes for wound healing and inflammation inhibition, *Bioact. Mater.* 6 (10) (2021) 3109–3124, <https://doi.org/10.1016/j.bioactmat.2021.02.006>.
- [40] D.C. Joshi, C.L. Zhang, D. Mathur, A. Li, G. Kaushik, Z.H. Sheng, S.Y. Chiu, Tripartite crosstalk between cytokine IL-1 $\beta$ , NMDA-R and misplaced mitochondrial anchor in neuronal dendrites is a novel pathway for neurodegeneration in inflammatory diseases, *J. Neurosci.* 42 (38) (2022) 7318–7329, <https://doi.org/10.1523/jneurosci.0865-22.2022>.
- [41] S.T. Smiley, M. Reers, C. Mottola-Hartshorn, M. Lin, A. Chen, T.W. Smith, G. D. Steele Jr., L.B. Chen, Intracellular heterogeneity in mitochondrial membrane potentials revealed by a J-aggregate-forming lipophilic cation JC-1, *Proc. Natl. Acad. Sci. U. S. A.* 88 (9) (1991) 3671–3675, <https://doi.org/10.1073/pnas.88.9.3671>.
- [42] B. Deng, S. Liu, Y. Wang, B. Ali, N. Kong, T. Xie, S. Koo, J. Ouyang, W. Tao, Oral nanomedicine: challenges and opportunities, *Adv. Mater.* (2023) e2306081, <https://doi.org/10.1002/adma.202306081>.
- [43] B. Lv, L. Lu, L. Hu, P. Cheng, Y. Hu, X. Xie, G. Dai, B. Mi, X. Liu, G. Liu, Recent advances in GelMA hydrogel transplantation for musculoskeletal disorders and related disease treatment, *Theranostics* 13 (6) (2023) 2015–2039, <https://doi.org/10.7150/thno.80615>.
- [44] X. Hu, X. Tian, C. Yang, F. Ling, H. Liu, X. Zhu, M. Pei, H. Yang, T. Liu, Y. Xu, F. He, Melatonin-loaded self-healing hydrogel targets mitochondrial energy metabolism and promotes annulus fibrosus regeneration, *Mater Today Bio* 23 (2023) 100811, <https://doi.org/10.1016/j.mtbio.2023.100811>.
- [45] H. Chen, A. Hu, M. Xiao, S. Hong, J. Liang, Q. Zhang, Y. Xiong, M. Gu, C. Mu, Preliminary delivery efficiency prediction of nanotherapeutics into crucial cell populations in bone marrow niche, *Asian J. Pharm. Sci.* 18 (6) (2023) 100868, <https://doi.org/10.1016/j.ajps.2023.100868>.
- [46] Y. Zhang, A. Khalique, X. Du, Z. Gao, J. Wu, X. Zhang, R. Zhang, Z. Sun, Q. Liu, Z. Xu, et al., Biomimetic design of mitochondria-targeted hybrid nanozymes as superoxide scavengers, *Adv. Mater.* 33 (9) (2021) e2006570, <https://doi.org/10.1002/adma.202006570>.
- [47] Y. Zhang, H. Zhang, F. Zhao, Z. Jiang, Y. Cui, M. Ou, L. Mei, Q. Wang, Mitochondrial-targeted and ROS-responsive nanocarrier via nose-to-brain pathway for ischemic stroke treatment, *Acta Pharm. Sin. B* 13 (12) (2023) 5107–5120, <https://doi.org/10.1016/j.apsb.2023.06.011>.
- [48] X. Pi, J. Liu, Y. Sun, Q. Ban, J. Cheng, M. Guo, Protein modification, IgE binding capacity, and functional properties of soybean protein upon conjugation with polyphenols, *Food Chem.* 405 (Pt A) (2023) 134820, <https://doi.org/10.1016/j.foodchem.2022.134820>.
- [49] Y. Wang, J. Zhou, X. Tian, L. Bai, C. Ma, Y. Chen, Y. Li, W. Wang, Effects of covalent or noncovalent binding of different polyphenols to acid-soluble collagen on protein structure, functionality, and digestibility, *J. Agric. Food Chem.* 71 (48) (2023) 19020–19032, <https://doi.org/10.1021/acs.jafc.3c06510>.
- [50] E. Kaschak, A.C. Goedert, L. Igarashi-Mafra, M.R. Mafra, Effect of divalent cations on bovine serum albumin (BSA) and tannic acid interaction and its influence on turbidity and in vitro protein digestibility, *Int. J. Biol. Macromol.* 136 (2019) 486–492, <https://doi.org/10.1016/j.ijbiomac.2019.06.102>.
- [51] N. Zhang, W. Zeng, Y. Xu, R. Li, M. Wang, Y. Liu, S. Qu, K.W. Ferrara, Z. Dai, Pyroptosis induction with nanosensitizer-augmented sonodynamic therapy combined with PD-L1 blockade boosts efficacy against liver cancer, *Adv. Healthcare Mater.* (2023) e2302606, <https://doi.org/10.1002/adhm.202302606>.
- [52] Y. Yang, P.Y. Liu, W. Bao, S.J. Chen, F.S. Wu, P.Y. Zhu, Hydrogen inhibits endothelial cancer growth via a ROS/NLRP3/caspase-1/GSDMD-mediated pyroptotic pathway, *BMC Cancer* 20 (1) (2020) 28, <https://doi.org/10.1186/s12885-019-6491-6>.
- [53] R. Miao, C. Jiang, W.Y. Chang, H. Zhang, J. An, F. Ho, P. Chen, H. Zhang, C. Junqueira, D. Amgalan, et al., Gasdermin D permeabilization of mitochondrial inner and outer membranes accelerates and enhances pyroptosis, *Immunity* 56 (11) (2023) 2523–2541, <https://doi.org/10.1016/j.immuni.2023.10.004>.
- [54] Y. Chen, R. Luo, J. Li, S. Wang, J. Ding, K. Zhao, B. Lu, W. Zhou, Intrinsic radical species scavenging activities of tea polyphenols nanoparticles block pyroptosis in endotoxin-induced sepsis, *ACS Nano* 16 (2) (2022) 2429–2441, <https://doi.org/10.1021/acsnano.1c08913>.
- [55] Y.L. Wu, C.H. Zhang, Y. Teng, Y. Pan, N.C. Liu, P.X. Liu, X. Zhu, X.L. Su, J. Lin, Propionate and butyrate attenuate macrophage pyroptosis and osteoclastogenesis induced by CoCrMo alloy particles, *Mil Med Res* 9 (1) (2022) 46, <https://doi.org/10.1186/s40779-022-00404-0>.
- [56] L. Wang, R. Deng, S. Chen, R. Tian, M. Guo, Z. Chen, Y. Zhang, H. Li, Q. Liu, S. Tang, H. Zhu, Carboxypeptidase A4 negatively regulates HGS-ETR1/2-induced pyroptosis by forming a positive feedback loop with the AKT signalling pathway, *Cell Death Dis.* 14 (12) (2023) 793, <https://doi.org/10.1038/s41419-023-06327-5>.
- [57] V.A.K. Rathinam, Y. Zhao, F. Shao, Innate immunity to intracellular LPS, *Nat. Immunol.* 20 (5) (2019) 527–533, <https://doi.org/10.1038/s41590-019-0368-3>.
- [58] Y. Li, L.H. Chang, W.Q. Huang, H.W. Bao, X. Li, X.H. Chen, H.T. Wu, Z.Z. Yao, Z. Z. Huang, S.E. Weinberg, et al., IL-17A mediates pyroptosis via the ERK pathway and contributes to steroid resistance in CRSwNP, *J. Allergy Clin. Immunol.* 150 (2) (2022) 337–351, <https://doi.org/10.1016/j.jaci.2022.02.031>.
- [59] H. Xing, Z. Zhang, Q. Mao, C. Wang, Y. Zhou, X. Zhou, L. Ying, H. Xu, S. Hu, N. Zhang, Injectable exosome-functionalized extracellular matrix hydrogel for metabolism balance and pyroptosis regulation in intervertebral disc degeneration, *J. Nanobiotechnol.* 19 (1) (2021) 264, <https://doi.org/10.1186/s12951-021-00991-5>.
- [60] D. Zheng, W. Chen, T. Chen, X. Chen, J. Liang, H. Chen, H. Shen, L. Deng, H. Ruan, W. Cui, Hydrogen ion capturing hydrogel microspheres for reversing inflammation, *Adv. Mater.* (2023) e2306105, <https://doi.org/10.1002/adma.202306105>.
- [61] H. Xu, Z.H. Dai, G.L. He, H.C. Cai, X.Y. Chen, Y.L. Chen, C. Xu, S.R. Sheng, Gamma-oryzanol alleviates intervertebral disc degeneration development by intercepting the IL-1 $\beta$ /NLRP3 inflammasome positive cycle, *Phytomedicine* 102 (2022) 154176, <https://doi.org/10.1016/j.phymed.2022.154176>.
- [62] J. Shen, A. Chen, Z. Cai, Z. Chen, R. Cao, Z. Liu, Y. Li, J. Hao, Exhausted local lactate accumulation via injectable nanozyme-functionalized hydrogel microsphere for inflammation relief and tissue regeneration, *Bioact. Mater.* 12 (2022) 153–168, <https://doi.org/10.1016/j.bioactmat.2021.10.013>.
- [63] Z. Wang, H. Yang, X. Xu, H. Hu, Y. Bai, J. Hai, L. Cheng, R. Zhu, Ion elemental-optimized layered double hydroxide nanoparticles promote chondrogenic differentiation and intervertebral disc regeneration of mesenchymal stem cells through focal adhesion signaling pathway, *Bioact. Mater.* 22 (2023) 75–90, <https://doi.org/10.1016/j.bioactmat.2022.08.023>.
- [64] Y.J. Che, J.B. Guo, T. Liang, X. Chen, W. Zhang, H.L. Yang, Z.P. Luo, Assessment of changes in the micro-nano environment of intervertebral disc degeneration based on Pflrmm9 grade, *Spine J.* 19 (7) (2019) 1242–1253, <https://doi.org/10.1016/j.spinee.2019.01.008>.
- [65] G. Zuo, P. Zhuang, X. Yang, Q. Jia, Z. Cai, J. Qi, L. Deng, Z. Zhou, W. Cui, J. Xiao, Regulating chondro-bone metabolism for treatment of osteoarthritis via high-permeability micro/nano hydrogel microspheres, *Adv. Sci.* (2023) e2305023, <https://doi.org/10.1002/advs.202305023>.